nature communications

Article

https://doi.org/10.1038/s41467-025-67580-0

A bio-adaptive physical hydrogel enables dynamic tissue engineering for tracheal reconstruction

Received: 25 April 2025

Accepted: 3 December 2025

Published online: 14 December 2025

Check for updates

Hai Tang[1,2,6], Hanchen Wang[3,6], Weiyan Sun[1,2,6] ✉, Yi Chen[1,2,6], Ziyin Pan[1,2], Qingfeng Bai[1,2], Yaoben Wang[3], Weikang Lin[1,2], Yulong Hu[1,2], Lei Wang[1,2], Minglei Yang[4], Guofang Zhao[4], Lei Zhang[1,2], Yunlang She[1,2], Xuefei Hu[1,2], Kewen Lei[5], Jiandong Ding[3], Lin Yu[3] ✉ & Chang Chen[1,2] ✉

Organ functionalization is inherently complex and dynamic, involving multi-layered tissue structures and continuous cellular remodeling. To address the clinical need for long-segment tracheal reconstruction, we propose a dynamic tissue engineering (DTE) strategy using a bio-adaptive physical hydrogel (BP-Gel) to emulate native tracheal development and enable dynamic regeneration of key tissue components. Here we show that chondrocytes cultured within BP-Gel form cartilage rings through an embryo-like chondrification process, during which the gel's percolation network adapts to cell migration and aggregation. The resulting cartilage exhibits a native-like multilayered morphology that enhances mechanical stability and resists degradation. Before transplantation, BP-Gel loaded with anti-inflammatory cytokines (IL-Gel) is introduced into inter-ring spaces to suppress inflammation and promote vascularization and epithelial maturation. In a rabbit tracheal defect model, this strategy reconstructs a functional trachea mimicking native structure and physiology, offering a promising, clinically relevant route to tracheal reconstruction.

Long-segment tracheal defects caused by tumors, infections, or congenital diseases are often associated with life-threatening complications, leading to a severe impairment in patients' quality of life and increased mortality rates[1–4]. In such cases, tracheal replacement remains the sole viable therapeutic option to save lives[5,6]. Despite this urgent need, no clinically approved trachea substitutes are currently available. The native trachea has a complex structure featuring cartilage rings for radial support, a transmural blood supply, and a defensive airway epithelium. Although a biomimetic tracheal substitute incorporating those functional elements has been developed and has shown promising results in preclinical studies[7,8], several challenges still hinder its clinical application. For example, the cartilage tissue generated via traditional scaffold-seeding methods lacks the intricate structural complexity of native cartilage, posing a risk of degradation during long-term implantation. Therefore, the trachea substitutes reconstructed from these artificial cartilages are vulnerable to loss of function due to structural collapse, which is further exacerbated by local inflammation or foreign body reactions.

In higher organisms, the formation and functional development of native organs are driven by a dynamic process in which the proliferation and migration of diverse cell types are regulated in a spatiotemporal-dependent manner, followed by the secretion of

[1]Department of Thoracic Surgery, Shanghai Pulmonary Hospital, Tongji University School of Medicine, Shanghai, China. [2]Shanghai Engineering Research Center of Lung Transplantation, Shanghai, China. [3]State Key Laboratory of Molecular Engineering of Polymers, Department of Macromolecular Science, Fudan University, Shanghai, China. [4]Department of Cardiothoracic Surgery, Ningbo No.2 Hospital, Ningbo, Zhejiang, China. [5]Koch Institute for Integrative Cancer Research, Massachusetts Institute of Technology, Cambridge, MA, USA. [6]These authors contributed equally: Hai Tang, Hanchen Wang, Weiyan Sun, Yi Chen. ✉e-mail: sweiyan1@163.com; yu_lin@fudan.edu.cn; changchenc@tongji.edu.cn

extracellular matrix (ECM) proteins and gene-phenotype transformations[9–11]. These dynamic processes result in continuous changes in the physical or biochemical microenvironment in the extracellular space, which in turn guide the functional development and maturation of the entire organ[12,13]. Therefore, we propose a dynamic tissue engineering (DTE) strategy to recapture the dynamics of native organ development by exploiting bio-adaptive biomaterials or scaffolds that can actively and continuously interact with the developing tissue throughout the regeneration window. However, to date, few biomaterials or scaffolds have been designed to coordinate with cellular or tissue dynamics in their microenvironment to enable the biomimetic reconstruction of complex organs like the trachea[14,15].

Hydrogels possess a three-dimensional (3D) polymer network architecture that mimics the native ECM and can serve as reservoirs for the sustained delivery of bioactive therapeutics[16,17]. They have been widely utilized in organ/tissue regeneration and drug delivery[18,19]. In contrast to stable 3D networks in chemically-crosslinked hydrogels, a gel network formed by weak physical interactions, e.g., hydrophobic interactions and host-guest interactions, easily undergoes dynamic changes in response to external stimuli[20,21]. The flexible, physically crosslinked network allows cells to actively remodel their niche for optimal cellular proliferation, migration, differentiation, and subsequent tissue growth and development[19,22].

Inspired by these findings, a bio-adaptive physical hydrogel (BP-Gel) composed of thermosensitive and biodegradable poly(lactic acid-co-glycolic acid)-poly(ethylene glycol)-poly(lactic acid-co-glycolic acid) (PLGA-PEG-PLGA) triblock copolymers was developed to reconstruct a native-like trachea in this study. BP-Gel is a free-flowing sol at room temperature and spontaneously turns into a semi-solid physical hydrogel at body temperature mediated by enhanced hydrophobic interactions. The sol–gel transition behavior and adaptive percolated network of BP-Gel offer a thermally responsive and mechanically adaptive platform well-suited for dynamic structural rearrangement during trachea regeneration. Furthermore, BP-Gel also enables mild and efficient encapsulation of interleukin molecules while achieving sustained release in situ, thereby establishing precise immune niches conducive to trachea regeneration (Fig. 1a).

Specifically, the physical percolation network in the BP-Gel could dynamically adapt to the migration, proliferation, and aggregation of chondrocytes, thus facilitating the fusion of chondrocyte clusters into large aggregates. This procedure resembles the embryo-like chondrification process, in which undifferentiated mesenchymal cells migrate, proliferate, and condense to form cartilage primordia[23–25]. This dynamically adaptive culture environment induced a native-like stratified morphology in the engineered cartilage, resulting in enhanced mechanical properties and improved resistance to degradation in vivo. We refer to this type of cartilage as biomimetic cartilage (BioC) because it shares both structural and functional similarities with native tracheal cartilage. Cartilage rings derived from BioC were thus employed as the main mechanical support for trachea reconstruction. Next, to generate a dynamic regenerative niche, a second BP-Gel loaded with the anti-inflammatory cytokines interleukin-4 (IL-4)/IL-13 (denoted as IL-Gel) was applied to seal the interstices between BioC rings before heterotopic transplantation into the platysma muscle. Continuous interleukin delivery activated an immune cell-mediated cascade that substantially reduced local inflammation while stimulating coordinated regeneration of trachea components, including the formation of transmural vascular networks and the development of airway epithelium. After four weeks of dynamic reconstruction in vivo, a native-like trachea substitute was expeditiously obtained for implantation into the recipient. Finally, the long-term functionality and translational potential of the trachea substitute were extensively evaluated using a rabbit tracheal defect model.

Results

Fabrication and characterization of BP-Gel and IL-Gel

The triblock copolymer PLGA-PEG-PLGA, whose molecular structure is shown in Supplementary Fig. 1a, was synthesized by ring-opening copolymerization of D,L-lactide and glycolide using PEG as the macroinitiator. ^{1}H nuclear magnetic resonance (^{1}H-NMR) analysis verified that the number average molecular weight of PLGA-PEG-PLGA was 1750-1500-1750 and the ratio of lactic acid to glycolic acid in PLGA blocks was 3.2:1 (Supplementary Fig. 1b). Gel permeation chromatography (GPC) confirmed that the molar mass dispersity ($Đ_m$) of the synthesized copolymers was 1.23 (Supplementary Fig. 1c).

The gelation mechanism of BP-Gel is attributed to the self-assembly of PLGA-PEG-PLGA polymers to micelles with PEG as the shells and PLGA as the cores in water, followed by the formation of a percolated micelle network via temperature-induced micelle aggregation[17], as illustrated in Fig. 1b. This result was further confirmed by transmission electron microscopy (TEM) observations (Fig. 1c) and dynamic light scattering measurements (Supplementary Fig. 1d). When the polymer concentration reached 5 wt% or above, the PLGA-PEG-PLGA polymers were soluble in water at low or room temperatures and underwent a sol–gel transition as the temperature increased, as presented in Fig. 1d. Furthermore, dynamic rheological measurements showed that the BP-Gel system composed of 12.5 wt% polymer aqueous solution indeed exhibited a sol-to-gel transition upon heating (Supplementary Fig. 1e) and formed a stable gel at body temperature (37 °C) (Supplementary Fig. 1f). Moreover, as the polymer concentration increased, the phase transition temperature decreased and the modulus of the gel formed at 37 °C increased (Fig. 1d and Supplementary Fig. 1g).

Subsequently, Live/Dead staining assays demonstrated that the proliferation of cells was not affected by treatment with 1 wt% PLGA-PEG-PLGA solution, indicating the good cytocompatibility of the synthesized copolymer. Live/Dead staining with Hoechst 33342 confirmed high cell viability (Supplementary Fig. 1h) and enabled the visualization of cell nuclei. Ki-67 immunofluorescence (IF) staining on Days 1, 4, and 7 showed comparable proliferative activity among control, GelMA, and BP-Gel groups, supported by quantification of Ki-67-positive cells (Supplementary Fig. 1i, j). Cell number counting, DNA content, and Cell Counting Kit-8 (CCK-8) assays further confirmed the lack of significant differences in proliferation across groups (Supplementary Fig. 1k–m). In addition, BP-Gel with a polymer mass fraction of 25 wt% was subcutaneously injected into the dorsal region of ICR mice to assess its in vivo degradability. Anatomical observations and weighting analysis revealed that the BP-Gel system was maintained in vivo for over one month (Supplementary Fig. 1n). Non-invasive fluorescence imaging also supported these findings (Supplementary Fig. 1o).

The interleukin molecules IL-4 and IL-13, whose structures are illustrated in Supplementary Fig. 1p, were expediently encapsulated into BP-Gel composed of 25 wt% polymer solution by simply mixing them at the sol state, and the resulting system was known as IL-Gel. In vitro release tests showed that IL-4/13 could be continuously and steadily released from BP-Gel, with the cumulative release amount exceeding 80% within 4 weeks (Fig. 1e). Finally, the IL-Gel system containing Cy5.5-labeled interleukin molecules was subcutaneously injected into ICR mice, and the release of the drug in vivo was confirmed via intravital fluorescence imaging. As presented in Fig. 1f, g, the gradual decrease in fluorescence intensity indicated the slow and sustained release of interleukin molecules in vivo. In addition, routine blood and biochemical tests showed that the implantation of IL-Gel and subsequent release of interleukin molecules caused no adverse systemic effects (Supplementary Fig. 2).

Construction and characterization of BioC

BioC was constructed by seeding chondrocytes into BP-Gel (12.5 wt%) and culturing them in chondrogenic medium, with GelMA as a control.

https://doi.org/10.1038/s41467-025-67580-0

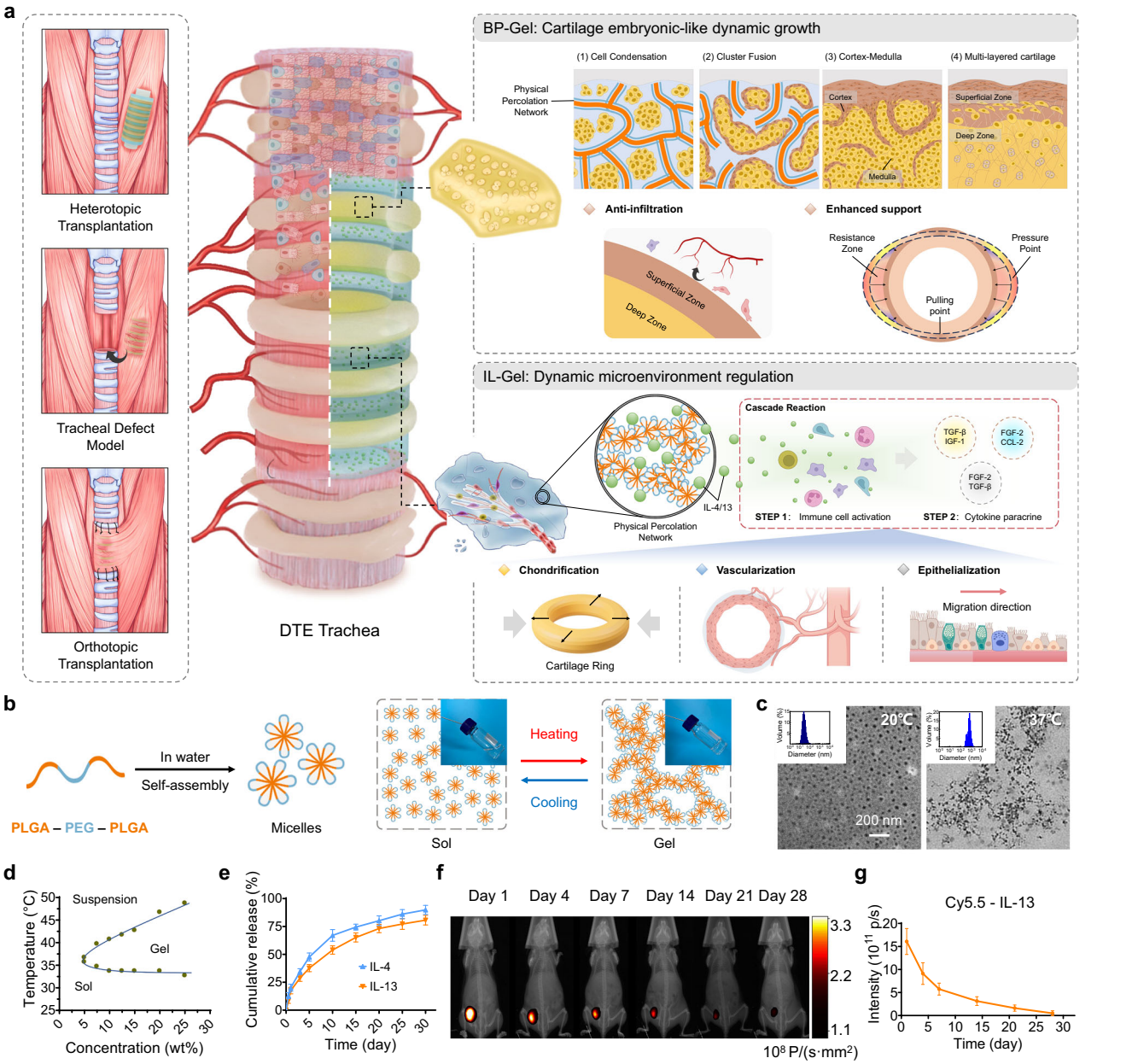

Fig. 1 | Tracheal reconstruction strategy and characterization of the BP-Gel. **a** DTE tracheal construction strategy: (i) The substitute comprises BioC rings (chondrocytes cultured in BP-Gel) and IL-Gel (BP-Gel loaded with interleukins). (ii) Ether bonds in BP-Gel generate a surface "water film" via hydrogen bonding, reducing adhesion and promoting cell clustering to mimic embryonic development. (iii) IL-Gel enables sustained interleukin release to induce macrophage polarization and immune cascade activation, maintaining cartilage phenotype, stimulating angiogenesis, and promoting epithelial migration. Elements were created in BioRender. Tang, H. (2025) https://BioRender.com/slb7t02. **b** Schematic of PLGA-PEG-PLGA micelle formation and heat-induced sol–gel transition. **c** TEM images of micelles at two temperatures ($n = 3$ individual samples). **d** Phase diagram of BP-Gel. **e** In vitro IL-4/13 release from IL-Gel ($n = 3$ individual samples per group). **f** Representative fluorescence micrographs of ICR mice at the indicated time points after subcutaneous injection of IL-Gel containing Cy5.5-labeled IL-13. **g** Fluorescence intensity over time ($n = 3$ individual samples). The data are expressed as the mean ± s.d. BP-Gel, bio-adaptive physical hydrogel. IL-Gel, interleukin-loaded BP-Gel. Source data is provided as a Source data file.

Concentration screening (6.25–25 wt%) showed that low concentrations led to structural instability and cell sedimentation, while high concentrations produced excessive stiffness and reduced porosity, resulting in scattered cells. Thus, 12.5 wt% was selected as the working concentration (Supplementary Fig. 3a). BP-Gel also maintained stable gelation at 37 °C with gradual degradation, unlike Pluronic F127, which degraded completely within 72 h (Supplementary Fig. 3b). Bright-field and confocal microscopy confirmed that chondrocytes aggregated into clusters in BP-Gel, whereas they remained scattered in GelMA (Fig. 2a and Supplementary Fig. 4a). Quantitative analysis further confirmed that the number of chondrocyte clusters in BP-Gel was significantly greater than that in GelMA at all observation points (Fig. 2b). This interesting phenomenon of spontaneous chondrocyte aggregation in BP-Gel was also verified by a dynamic video (Supplementary Movie 2). Based on this, a schematic of cell growth status in the two different gel systems is proposed, as displayed in Fig. 2c.

BP-Gel was formed by the aggregation of micelles, in which hydrophilic PEG segments containing many ether bonds constituted the shells of the micelles and were exposed to the aqueous environment. We speculate that numerous water molecules bind to the PEG

https://doi.org/10.1038/s41467-025-67580-0

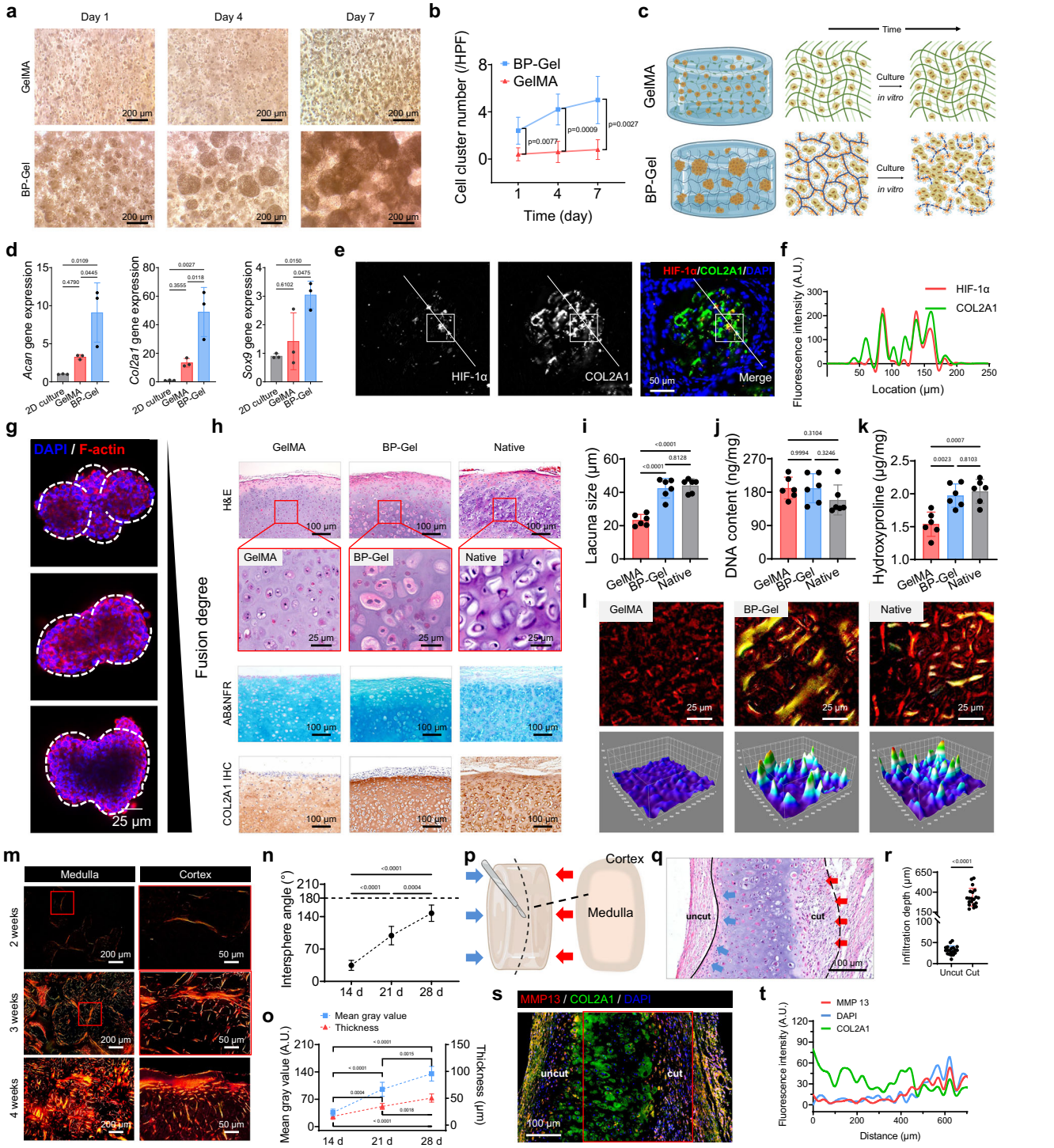

shells via hydrogen bonding, creating an anti-adhesion microenvironment[26,27], as illustrated in Supplementary Fig. 4b. This microenvironment prevents chondrocytes from adhering to the gel network, thereby forcing them to aggregate. To verify this hypothesis, chondrocytes were cultured on the surface of BP-Gel. As expected, unlike the chondrocytes cultured on ordinary plates (2D culture), the cells grown on the BP-Gel surface did not adhere well, resulting in the formation of regular spherical shapes (Supplementary Fig. 4c).

We subsequently evaluated the expression of adhesion-related genes (*Lama*, *Fn1*, *Cdh2*, and *Gja1*) (Supplementary Fig. 4d) and cartilage-related genes (*Acan*, *Col2a1*, and *Sox9*) (Fig. 2d). The results showed that the expression levels of these genes in chondrocytes grown in BP-Gel were significantly up-regulated compared with those cultured on plates or in GelMA, indicating that culturing chondrocytes in BP-Gel promotes their aggregation and fusion, thus facilitating cartilage formation. Consistently, Western blotting confirmed higher levels of adhesion-related proteins in the BP-Gel group, and Hematoxylin and Eosin (H&E) and IF staining further demonstrated markedly stronger expression of Laminin subunit alpha-1 (LAMA1), Fibronectin (FN1), N-cadherin (CDH2), and Connexin-43 (GJA1), with quantitative analysis showing significant increases in all four markers (Supplementary Fig. 4e–h).

Next, we explored the process of chondrocyte development in BioC. IF staining revealed that the expression of Collagen type II alpha 1

Fig. 2 | Construction and dynamic development of BioC. a Growth state of chondrocytes in BP-Gel and GelMA over culture time under bright-field microscopy. **b** Quantification of chondrocyte clusters in BP-Gel and GelMA ($n = 5$ individual samples per group). **c** Schematic illustrating aggregated (BP-Gel) versus scattered (GelMA) growth states. Elements were created in BioRender. Tang, H. (2025) https://BioRender.com/mkdsv40. **d** Expression of cartilage-associated genes after 7 days of culture; 2D control: cells on standard plates ($n = 3$ individual samples per group). **e**, **f** Confocal images and colocalization analysis of HIF-1α (red) and COL2A1 (green) in BP-Gel. **g** Representative micrographs showing fusion of chondrocyte clusters in BP-Gel. **h** Representative H&E, AB&NFR, and COL2A1 IHC staining micrographs of tissue at 4 weeks post-implantation. **i** Quantitative analysis of cartilage lacuna size ($n = 6$ random fields from 3 individual samples per group). **j**, **k** DNA and hydroxyproline content of tissues at 4 weeks post-implantation ($n = 6$ values from 3 individual samples with 2 technical replicates per group). **l** Representative SR-stained micrographs of tissue at 4 weeks post-implantation. **m**–**o** Polarizing SR staining at indicated time points, and quantitative analysis of intersphere angle, fluorescence intensity, and cortex thickness, red boxes indicate developing cartilage cortex. ($n = 6$ random fields from 3 individual samples per group). **p** Schematic of BioC bisection exposing the medulla. Elements were created in BioRender. Tang, H. (2025) https://BioRender.com/cku0oog. **q** Representative H&E-stained BioC retaining a unilateral cortical. **r** Quantification of tissue invasion depth on cortical (uncut) versus non-cortical (cut) sides ($n = 20$ random fields from 3 individual samples per group). **s**, **t** IF staining and colocalization analysis of MMP13 (red) and COL2A1 (green) in BioC with a unilateral cortical at 4 weeks post-implantation. Representative images in (**e**), (**g**), (**h**), and (**l**) were selected from 3 individual samples per group. The data are expressed as mean ± s.d. Data in (**b**) and (**r**) were analyzed by two-tailed Student's t-test. Data in (**d**), (**i**), (**j**), (**k**), (**n**), and (**o**) were analyzed by one-way ANOVA followed by Bonferroni's post hoc test. Source data is provided as a Source data file.

chain (COL2A1) and Hypoxia-inducible factor 1-alpha (HIF-1α) was significantly increased within the chondrocyte clusters formed in BP-Gel (Fig. 2e and Supplementary Fig. 5a, showing an amplified region of Fig. 2e). Colocalization analysis based on protein expression intensity demonstrated that the expression levels of these two proteins were highly coincident (Fig. 2f and Supplementary Fig. 5b). To further substantiate this point, we examined cell spheroids, a recognized model of chondrocyte development. IF staining showed high expression of HIF-1α and COL2A1 in cell spheroids, which closely resembled the expression patterns observed in BioC cultured within BP-Gel (Supplementary Fig. 5c). These findings, combined with previous studies[28–30], suggest that the formation of chondrocyte clusters creates a hypoxic environment and stimulates the expression of HIF-1α, which in turn promotes the development of chondrocytes and the secretion of the cartilage matrix. Similarly, immunohistochemical (IHC) staining manifested that Yes-associated protein 1 (YAP), a protein that regulates matrix secretion in response to mechanical signaling to promote cartilage development and tissue remodeling, was expressed at higher levels in chondrocyte clusters compared with the surrounding scattered chondrocytes (Supplementary Fig. 5d). Building on these findings, we performed additional IF staining of chondrogenic markers using GelMA as a control and cell spheroids as a reference. Chondrocytes cultured in BP-Gel showed markedly stronger SOX9 and COL2A1 expression than those in GelMA, with quantification confirming higher SOX9 and COL2A1 levels and an increased proportion of SOX9-positive cells (Supplementary Fig. 5e–h). These results further demonstrate that the BP-Gel microenvironment promotes chondrogenic differentiation and cartilage matrix deposition.

Additionally, we found that when chondrocyte clusters formed in BP-Gel, they tended to further fuse into larger chondrocyte aggregates as the incubation time extended. This fusion further promoted the secretion of the cartilage matrix, leading to the formation of native-like cartilage tissue (Supplementary Fig. 6a). To further elucidate the early chondrogenic process within BP-Gel constructs, we analyzed 2-week samples and compared them with embryonic tracheal cartilage, which represents a developmental benchmark of native chondrogenesis. Specifically, histological analyses of mice embryonic trachea at E12.5, E14.5, and E16.5 using H&E, Alcian Blue-Nuclear Fast Red (AB&NFR), Safranin O-Fast Green (SO&FG), and SOX9 IF revealed progressive mesenchymal condensation and early matrix deposition, thereby providing a reference for evaluating the developmental stage of BP-Gel-induced cartilage (Supplementary Fig. 6b). Figure 2g shows a typical fusion process where small chondrocyte clusters fused into a larger chondrocyte cluster. Conversely, the chondrocytes cultured in GelMA remained dispersed throughout a 4-week in vitro culture period (Supplementary Fig. 6a). These encouraging findings are attributed to the weak physical gel network formed in BP-Gel and the presence of micelles with numerous exposed PEG shells, which provide a dynamic adaptive environment that facilitates the aggregation and fusion of chondrocytes. In contrast, the robust chemically-crosslinked gel network in GelMA and its slow in vitro degradation result in the firm immobilization of chondrocytes within the hydrogel matrix, thereby hindering their aggregation and subsequent fusion.

Encouraged by these in vitro results, BioC samples that had been cultured in vitro for 4 weeks were implanted subcutaneously into nude mice. Following this process, BioC gradually began to resemble native cartilage. Histological analyses confirmed that after 4 weeks of in vivo culture, the collected BioC exhibited cartilage-specific extracellular matrix (ECM) deposition, as demonstrated by H&E, AB&NFR, and COL2A1 IHC staining, which qualitatively assessed tissue morphology, GAG-rich matrix deposition, and chondrogenic zonal distribution (Fig. 2h). Quantitative detection of the cartilage lacunae size in each group disclosed that the cartilage structure formed in BP-Gel was similar to that of natural cartilage (Fig. 2i). Measurements of DNA and hydroxyproline contents suggested that BioC has biochemical characteristics comparable to those of native cartilage (Fig. 2j, k).

Supplementary Fig. 7a–e presents macroscopic views, histological staining images and biochemical parameters of BioC at 2 and 4 weeks post-implantation. The continuous increase in lacunae structures and matrix content reflected the gradual maturation of cartilage in BP-Gel.

Native cartilage exhibits a distinct "cortex-medulla" structure, ensuring the structural integrity and functional adaptability required for cartilage development and load-bearing performance[31,32]. To further assess the structural organization of cartilage matrix, Sirius Red (SR) staining for COL2A1 and 3D reconstruction plots demonstrated that the distribution of COL2A1 within BioC based on BP-Gel closely resembled the characteristic grid-like COL2A1 arrangement in the native cartilage; however, no similar COL2A1 distribution was observed in GelMA (Fig. 2l). Moreover, the BioC samples obtained from different culture time points were also subjected to SR staining. As shown in Fig. 2m–o, SR staining of BioC at different growth stages revealed progressive fusion of chondrocyte clusters, continuous increase in COL2A1 deposition, and gradual thickening of the cortical layer, reflecting the dynamic formation of a "cortex-medulla" structure.

To elucidate the biological function of the formed cortical layer, BioC samples harvested after 4 weeks of in vivo culture were bisected and then implanted subcutaneously into nude mice (Fig. 2p). The side with an intact cortical layer exhibited well-preserved cartilaginous characteristics (Fig. 2q, r). In contrast, on the side devoid of the cortical layer, numerous surrounding cells had infiltrated into BioC, resulting in the degradation of cartilage. The results of IF staining further confirmed that the expression of COL2A1 was notably higher on the side with the retained cortex layer, while both cell density and Matrix metallopeptidase 13 (MMP13) expression markedly increased on the side where the cortex had been removed (Fig. 2s, t). These findings suggest that the formed cortical layer exerts a protective effect on inhibiting cartilage degradation.

Subsequently, tracheal BioC rings were obtained using a process similar to the construction of bulk BioC. Supplementary Fig. 7f and Supplementary Movie 1 show the macroscopic morphology of the generated tracheal BioC rings after different in vivo culture times. Mechanistic analysis further revealed that the "cortex-medulla" structure could effectively alleviate stress concentration within the ring architecture (Supplementary Fig. 7g). Notably, the stress concentration is detrimental to the stability of the trachea structure and can even lead to the collapse of the reconstructed trachea.

The ability of IL-Gel to induce macrophage polarization and modulate the local microenvironment in vivo

We designed a series of in vitro experiments to explore the local immunomodulatory effects induced by IL-Gel. M0 macrophages were utilized as the control, while the "LPS-M0 macrophage" model was used to mimic an inflammatory environment.

Cell morphology was first evaluated after various treatments (Supplementary Fig. 8a). Typically, M1 macrophages exhibit an irregular polygonal shape with many filopodia. In contrast, M2 macrophages display a spindle-like morphology characterized by prominent lamellipodia, resulting in a higher aspect ratio (Supplementary Fig. 8b). The results revealed that most of the macrophages exhibited an M2 phenotype after treatment with IL-Gel, with the highest aspect ratio (Supplementary Fig. 8a–c). Subsequently, we performed fluorescence staining of the cytoskeleton to visualize lamellipodia, and the statistical analysis of lamellipodium numbers was well consistent with the proportions of macrophage phenotypes in various groups (Supplementary Fig. 8d–f).

Figure 3a displays representative fluorescence micrographs of macrophages cultured in BP-Gel with or without IL-4/13, labeled with CD86 (a specific marker for M1 macrophages) and Macrophage mannose receptor (MMR) (a specific marker for M2 macrophages). Quantitative analysis revealed that the IL-Gel-stimulated macrophages exhibited reduced CD86 expression but the highest level of MMR expression (Fig. 3b). Subsequently, we analyzed these markers via flow cytometry (Fig. 3c), which demonstrated that IL-Gel induced less M1 phenotypic transformations but more M2 phenotypic transformations in macrophages (Supplementary Fig. 8g, h). Moreover, we performed PCR measurements to evaluate the expression of genes related to macrophage polarization under different induction conditions. The results showed that IL-Gel reduced the expression of M1 phenotype-related genes (*Tnf* and *Il1b*) while promoting the expression of M2 phenotype-related genes (*Il10* and *Mrc1*) (Fig. 3d).

The in vivo functions of IL-Gel were further evaluated after subcutaneous injection into ICR mice, and the treatment timeline is presented in Supplementary Fig. 8i. Supplementary Fig. 8j shows representative micrographs of H&E-stained slices of residual hydrogels containing surrounding tissues from 14 to 28 days post-injection. BP-Gel without IL-4/13 induced an acute inflammatory response, resulting in the infiltration of inflammatory cells into the surrounding tissue. In contrast, no obvious inflammatory cell infiltration was observed in the surrounding tissue of IL-Gel.

CD86/MMR IF staining was also performed on the surrounding tissues. The results revealed a higher proportion of M1 macrophages around IL-4/13-free BP-Gel, while more M2 macrophages were observed around IL-Gel (Supplementary Fig. 8k).

Subsequently, we performed IF staining using Lymphocyte antigen 6 complex locus G6D (Ly6G) (a specific marker for neutrophils) and CD45 (a specific marker for lymphocytes). The results demonstrated that the presence of IL-Gel significantly mitigated the infiltration of both lymphocytes and neutrophils, indicating its favorable anti-inflammatory effects (Supplementary Fig. 8l).

Furthermore, IF staining for the endothelial cell-related marker (Platelet/endothelial cell adhesion molecule 1, PECAM1) was conducted on the two groups. The IL-Gel group exhibited more functional blood vessels with an orderly arrangement (Supplementary Fig. 8m–o). These findings suggest that IL-Gel promotes endothelial cell growth. The results of tissue IHC staining also coincided with those of IF staining (Supplementary Fig. 9). Taken together, IL-Gel exerts a comprehensive regulatory effect on the microenvironment at the implantation site.

Enhanced development of cartilage, endothelium and epithelium in vitro through IL-Gel-induced immune cascades

We first established a co-culture system to examine the direct effects of IL-Gel on macrophage polarization, thereby confirming the ability of IL-4/13-loaded IL-Gel. We quantified cytokine levels in the culture medium of macrophages subjected to different treatments, as illustrated in Supplementary Fig. 10a. The results demonstrated that the presence of IL-4/13 significantly increased the concentrations of TGF-β1, TGF-β3, IGF-1, and bFGF in the culture medium (Fig. 3e). Additionally, treatment with IL-4/13 also reduced the secretion of CCL2. These findings suggest that IL-4/13-treated macrophages can release beneficial factors that promote tissue regeneration while mitigating inflammatory responses.

To mimic the in vivo microenvironment, building upon this, we further established a co-culture system to co-culture macrophages with chondrocytes, endothelial cells, or epithelial cells (Fig. 3f). The results illustrate the functional consequences of IL-Gel-induced macrophage polarization, demonstrating how polarized macrophages subsequently regulate the growth and development of chondrocytes, endothelial cells, and epithelial cells. First, we stained chondrocytes in the co-culture system with toluidine blue, revealing that IL-Gel-induced macrophage polarization promoted chondroitin production (Fig. 3g–i). Further IF staining of COL2A1 demonstrated that macrophage polarization significantly enhanced the development of chondrocytes (Fig. 3j, k). Similarly, the expression of cartilage-related genes, including COL2A1 and SOX9, was significantly up-regulated following IL-Gel stimulation (Supplementary Fig. 10b). These supportive data suggest that chondrocytes can differentiate and undergo chondrogenesis in response to IL-Gel-induced M2 macrophage polarization.

Subsequently, we investigated the effects of IL-Gel-induced macrophage polarization on the growth and development of human umbilical vein endothelial cells (HUVECs). Representative fluorescence micrographs of PECAM1 demonstrated that IL-Gel-induced macrophage polarization significantly promoted endothelial cell-related protein secretion (Fig. 3l, m). Meanwhile, the expression of endothelial cell-related genes (*PECAM1* and *VEGFA*) was also significantly up-regulated (Supplementary Fig. 10c). Moreover, scratch assays and tube formation assays discovered that the presence of IL-Gel substantially boosted the migratory ability of HUVECs (Supplementary Fig. 10d, e) and promoted angiogenesis (Supplementary Fig. 10f). These results suggest that IL-Gel facilitates well-organized angiogenesis.

Finally, we explored the effects of IL-Gel-induced macrophage polarization on the growth and development of epithelial cells in the co-culture system. Scratch assays revealed that there was no difference in the viability of epithelial cells under different co-culture conditions; however, IL-Gel-induced macrophage polarization significantly promoted the migration of epithelial cells (Supplementary Fig. 10g–j). In addition, to verify the impact of macrophage polarization on epithelial regeneration, Transwells were used to establish a air-liquid interface co-culture system (Fig. 3n). The results showed that the presence of IL-Gel significantly increased the protein expression of Keratin, type I cytoskeletal 14 (KRT14), a marker of epithelial stemness, and the expression of the epithelial ciliary marker acetylated tubulin (AC-Tub) (Fig. 3o). Scanning electron microscopy (SEM) observations also revealed enhanced ciliary coverage (Fig. 3o). Quantitative analysis further confirmed that IL-Gel significantly enhanced epithelial regeneration, characterized by the formation of a thicker membrane and more cilia (Fig. 3p, q).

https://doi.org/10.1038/s41467-025-67580-0

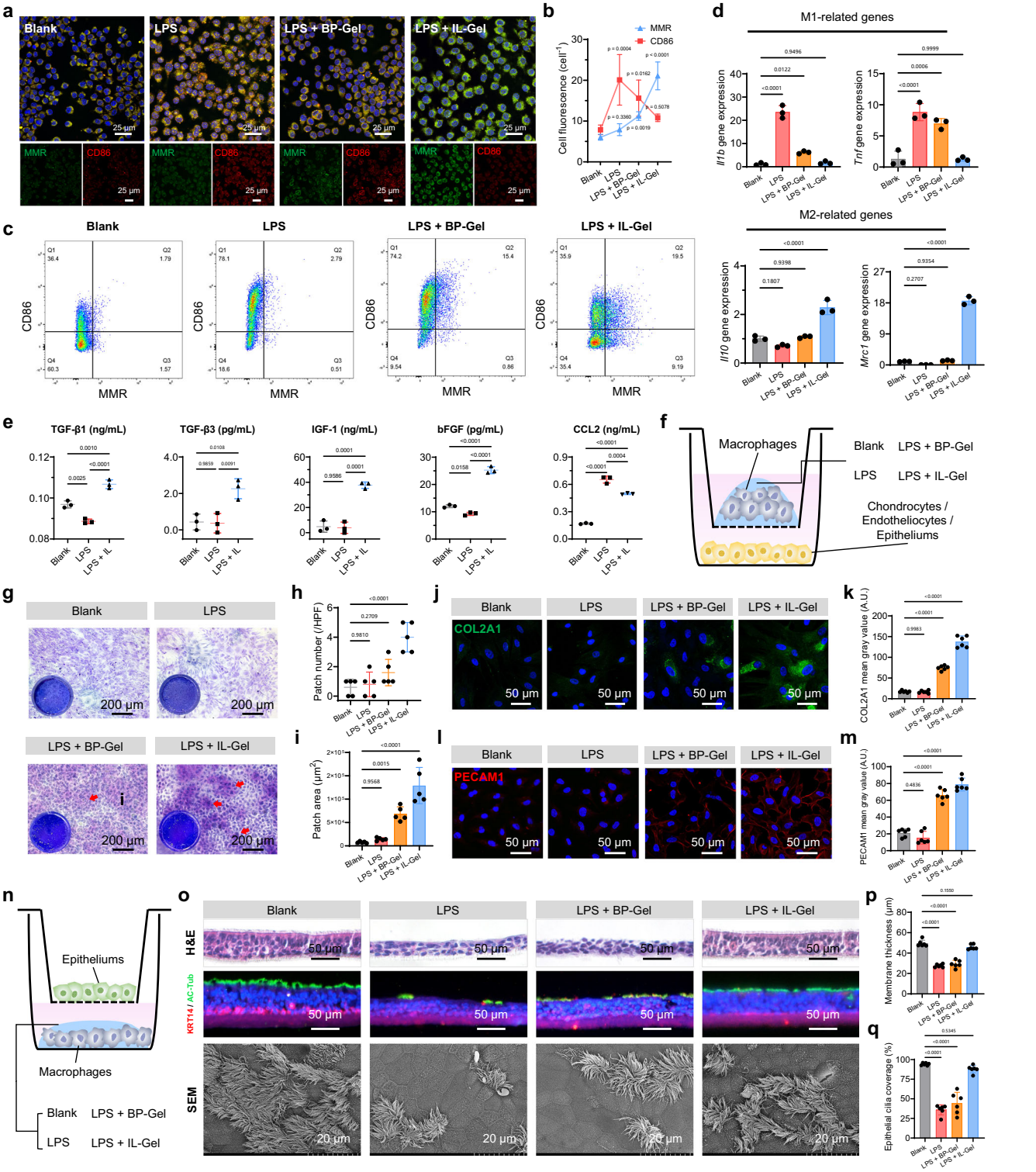

Promoted the phenotype maintenance and angiogenesis of BioC through IL-Gel-induced immune cascades in vivo

After a 4-week in vitro culture of chondrocyte-laden BP-Gel (BioC), the BioC was encapsulated with IL-Gel to form the BP@IL-Gel system, which was then implanted into the platysma muscle of rabbits, as shown in Fig. 4a. Given the anti-inflammatory effects of IL-Gel, this design is expected to create an anti-inflammatory environment around BioC (Fig. 4b). We also employed BioC (the BP-Gel group), chondrocyte-laden GeMA (the GelMA group) and chondrocyte-laden GeMA combined with cell-free GelMA coverage (the GelMA@Blk group) as the control groups (Fig. 4a and Supplementary Fig. 11a).

After 2 weeks of in vivo implantation, histological staining provided clear evidence of cartilage-specific matrix deposition. AB&NFR staining and COL2A1 IHC staining consistently showed that the BP@IL-Gel composite exhibited more cartilage-specific ECM deposition among the four groups (Fig. 4c and Supplementary Fig. 11b–d). To further quantify these observations, we analyzed cartilage lacunae based on the stained tissues and found that the number of lacunae was highest in the BP@IL-Gel group (Fig. 4d and Supplementary Fig. 11d). In

Fig. 3 | Effects of IL-Gel on macrophage polarization and subsequent effects of polarized macrophages on chondrocytes, endothelial cells, and epithelial cells. a, **b** Representative fluorescence micrographs and fluorescence intensity quantitative analysis of macrophages labeled with MMR (green) and CD86 (red) after 2 days of various treatments ($n = 5$ individual samples per group). **c** Flow cytometry analysis of macrophages after 2 days of various treatments. **d** Expression levels of M1-related (*Il1b* and *Tnf*) or M2-related (*Il10* and *Mrc1*) genes in macrophages after 2 days of various treatments ($n = 3$ individual samples per group). **e** Secreted levels of TGF-β1, TGF-β3, IGF, bFGF, and CCL2 in the macrophage culture medium after 7 days of treatment ($n = 3$ individual samples per group). **f** Schematic of the macrophage co-culture system. **g**–**i** Representative toluidine blue-stained micrographs and quantification of cartilage matrix patches in chondrocytes after 7 days of co-culture. The red arrows indicate the matrix accumulated ($n = 5$ random fields from 5 samples per group). **j**, **k** Representative fluorescence micrographs and quantitative analysis of COL2A1-labeled (green) chondrocytes after 7 days of co-culture ($n = 6$ random fields from 3 individual samples per group). **l**, **m** Representative fluorescence micrographs and quantitative analysis of PECAM1-labeled (red) endothelial cells after 7 days of co-culture ($n = 6$ random fields from 3 individual samples per group). **n** Schematic of the air-liquid interface co-culture system. **o** Representative fluorescence micrographs of epithelial cells labeled with KRT14 (red) and AC-Tub (green) after 7 days of co-culture in the air-liquid interface system and corresponding SEM images. **p**, **q** Quantitative analysis of membrane thickness and epithelial cilia coverage ($n = 6$ random fields from 3 individual samples per group. The data are expressed as mean ± s.d. Data were analyzed by one-way ANOVA followed by Bonferroni's post hoc test. Source data is provided as a Source Data file.

addition, biochemical assays of cartilage matrix demonstrated that relative glycosaminoglycan (GAG) and hydroxyproline contents were significantly elevated in the BP@IL-Gel group, indicating that this structural design effectively promoted maintenance of the cartilage phenotype and protected ectopic cartilage development (Fig. 4e and Supplementary Fig. 11e, f).

Subsequently, IF staining of CD86 and MMR was conducted to assess macrophage polarization in the vicinity of BP-Gel and BP@IL-Gel. The results demonstrated that, compared with the BP-Gel group, the BP@IL-Gel system induced a significant polarization of macrophages toward the M2 phenotype (Fig. 4f–h).

In addition, IF staining of COL2A1 and SOX9 and the corresponding quantitative analysis of COL2A1 revealed the obvious degradation of the cartilage matrix in the BP-Gel group (Fig. 4i). Conversely, the cartilage matrix was well-preserved in the BP-Gel group. SR staining further validated that the collagen arrangement in the BP@IL-Gel group exhibited a grid-like pattern, similar to that of native cartilage (Supplementary Fig. 11g, h). These results indicated that the chondrocytes in the BP@IL-Gel group were in a superior state than those in the BP-Gel group.

Staining of Actin, alpha 2, smooth muscle (α-SMA) can reflect cell infiltration and angiogenesis in the implant. As displayed in Fig. 4j, the absence of IL-4/13 cytokines in the BP-Gel group led to the growth of inflammation-induced blood vessels into the cartilage tissue, thereby promoting its degradation. Conversely, almost no blood vessels were observed within the cartilage tissue in the BP@IL-Gel group due to the sustained release of IL-4/13 from IL-Gel. Moreover, the increased vascular infiltration in the BP-Gel group made the cartilage more susceptible to ossification, as evidenced by SO&FG staining (Supplementary Fig. 11i). Collectively, these results suggest that IL-Gel facilitates well-organized angiogenesis while avoiding aberrant vascular infiltration into cartilage tissue.

Finally, we conducted an RNA-seq analysis of collected samples to determine the profile of immune-related gene expression (Fig. 4k). Pearson's correlation analysis revealed a significant correlation between the BP-Gel and BP@IL-Gel samples (Supplementary Fig. 11j). A heatmap of the differentially expressed mRNAs is shown in Fig. 4l. The volcano maps showed the differentially expressed genes (DEGs) between the two groups (Supplementary Fig. 11k). GO enrichment analysis indicated that the biological processes involved were primarily related to the regulation of the immune microenvironment (Fig. 4m). KEGG pathway analysis yielded similar results (Supplementary Fig. 11l). The immune-related biological processes and DEGs were integrated to construct a GOChord plot, revealing that THBS4, SLIT2, CAMK1D, and DAPK2 were the key genes in this process (Supplementary Fig. 11m). Additionally, we evaluated the relative expression of genes associated with crucial processes, including inflammation and angiogenesis. The analysis results indicate that BP@IL-Gel and BP-Gel exhibit distinct effects on modulating the inflammatory microenvironment and vascularization. The heat-map further allows a preliminary assessment of the up- or down-regulation trends of related genes (Fig. 4n).

DTE trachea-mediated segmental tracheal reconstruction

Multiple BioC rings that had been cultured in vitro for 4 weeks were superimposed and cast with IL-Gel to form a trachea substitute (called BP-Gel+IL-Gel), which was then heterotopically transplanted into the platysma muscle of rabbits for 4 weeks, achieving integration and vascularization. Afterwards, the trachea substitute was implanted to repair tracheal defects in rabbits (Fig. 5a). The trachea substitute constructed solely by superimposing multiple BioC rings served as the control group (called BP-Gel). A flow chart outlining the process for the fabrication of trachea substitute and subsequent segmental tracheal reconstruction is shown in Supplementary Fig. 12a.

Eight rabbits in each group underwent tracheal reconstruction surgery. In the BP-Gel group, none of the rabbits survived beyond 8 weeks. One rabbit died from tracheal obstruction following post-operative trachea hemorrhage, while the remaining seven succumbed to asphyxia caused by trachea collapse. In contrast, 62.5% of the rabbits in the BP@IL-Gel group survived beyond 8 weeks with stable respiration (Fig. 5b). In addition to the survival rate, the animals' respiration rate, heart rate, and blood oxygen (SaO_2) level were evaluated for up to 8 weeks post-surgery. The results indicated that the rabbits in the BP-Gel+IL-Gel group exhibited more favorable trends in these physiological parameters after tracheal reconstruction (Fig. 5c–e). Supplementary Tables 1 and 2 summarize the clinical outcomes of the DTE trachea-transplanted rabbits.

Figure 5f presents the surgical procedure, representative tracheoscopy images, and macrographs of the reconstructed trachea in the two groups. Supplementary Movies 3 and 4 demonstrate representative surgical procedures. In the BP-Gel group, the reconstructed trachea exhibited obvious collapse, whereas it remained patent in the BP-Gel+IL-Gel group. Quantitative analysis of the lumen inner diameter, tracheal length, and tracheal wall area revealed that the BP-Gel +IL-Gel group significantly outperformed the BP-Gel group and more closely resembled the native trachea (Fig. 5g, h and Supplementary Fig. 12b).

Figure 5i shows a longitudinal H&E-stained image of the native trachea. For the reconstructed trachea, longitudinal sections stained with H&E and AB&NFR are displayed in Fig. 5j. The results demonstrated that predominant cartilage degradation was found in the BP-Gel group. In contrast, the cartilage phenotype was well-preserved in the BP-Gel+IL-Gel group. Quantitative analysis of the cartilage area revealed that the cartilage retention rate in the BP-Gel+IL-Gel group was substantially higher than in the BP-Gel group (Fig. 5k). IHC staining of COL2A1 showed more deposition of the cartilage matrix in the BP-Gel+IL-Gel group (Fig. 5l, m). In addition, IF staining of epithelium-related markers (KRT14 and ZO-1) indicated significantly enhanced growth of the reconstructed tracheal epithelium in the BP-Gel+IL-Gel group compared with the BP-Gel group (Fig. 5n). Native rabbit trachea tissue stained with H&E, AB&NFR, COL2A1 (IHC), and KRT14 + ZO-1 (IF) served as reference standards, demonstrating that the BP-Gel+IL-Gel group exhibited cartilage content and epithelial organization more closely resembling native tissue. Consistently, staining of Keratin, type

https://doi.org/10.1038/s41467-025-67580-0

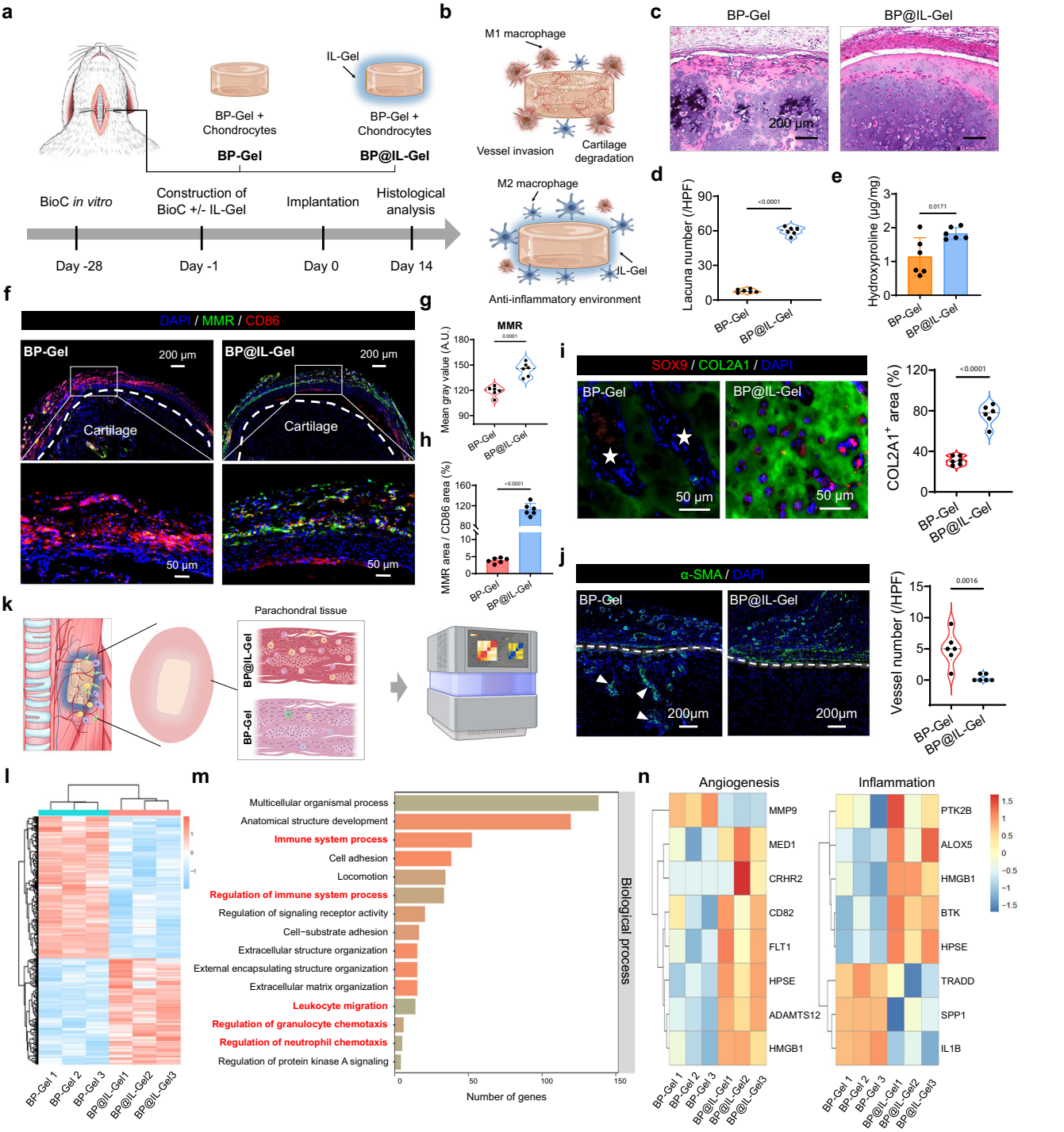

Fig. 4 | In vivo maintenance of cartilage phenotype of BioC and anti-angiogenesis in BioC through IL-Gel-induced macrophage polarization. **a** Schematic of the experimental design. Elements were created in BioRender. Tang, H. (2025) https://BioRender.com/vndpxvc. **b** Schematic of the immune niche around BioC in the BP-Gel and BP@IL-Gel groups. Elements were created in BioRender. Tang, H. (2025) https://BioRender.com/ae490p4. **c** Representative H&E-stained micrographs of tissue from different groups. **d** Quantitative analysis of the number of cartilage lacunae ($n = 6$ random fields from 3 individual samples per group). **e** Quantitative analysis of hydroxyproline content ($n = 6$ random fields from 3 individual samples per group). **f** Representative fluorescence micrographs labeled with MMR (green) and CD86 (red). **g**, **h** Quantitative analysis of MMR fluorescence intensity and of MMR/CD86 area ratio ($n = 6$ random fields from 3 individual samples per group). **i** Representative fluorescence micrographs labeled with SOX9 (red) and COL2A1 (green), and quantitative analysis of COL2A1-positive area. The white five-pointed stars indicate the degradation region of the cartilage matrix ($n = 6$ random fields from 3 individual samples per group). **j** Representative α-SMA (green) fluorescence micrographs and quantitative analysis of vessels number. The white triangles indicate the invasive blood vessels in cartilage tissue ($n = 6$ random fields from 3 individual samples per group). **k** Schematic of RNA-seq analysis of perichondral tissues obtained from different groups. Elements were created in BioRender. Tang, H. (2025) https://BioRender.com/x2t74di. **l** Heatmap of differentially expressed mRNAs identified via RNA-seq analysis in the BP-Gel and BP@IL-Gel groups ($n = 3$ individual samples per group). **m** GO analysis of the RNA-seq data from the BP-Gel and BP@IL-Gel groups. **n** Relative expression of genes related to crucial processes, including inflammation and angiogenesis, in the BP-Gel and BP@IL-Gel groups. The samples in different groups were collected 14 days post-implantation. The data are expressed as the mean ± s.d. Data were analyzed by two-tailed Student's t-test. Source data is provided as a Source data file.

https://doi.org/10.1038/s41467-025-67580-0

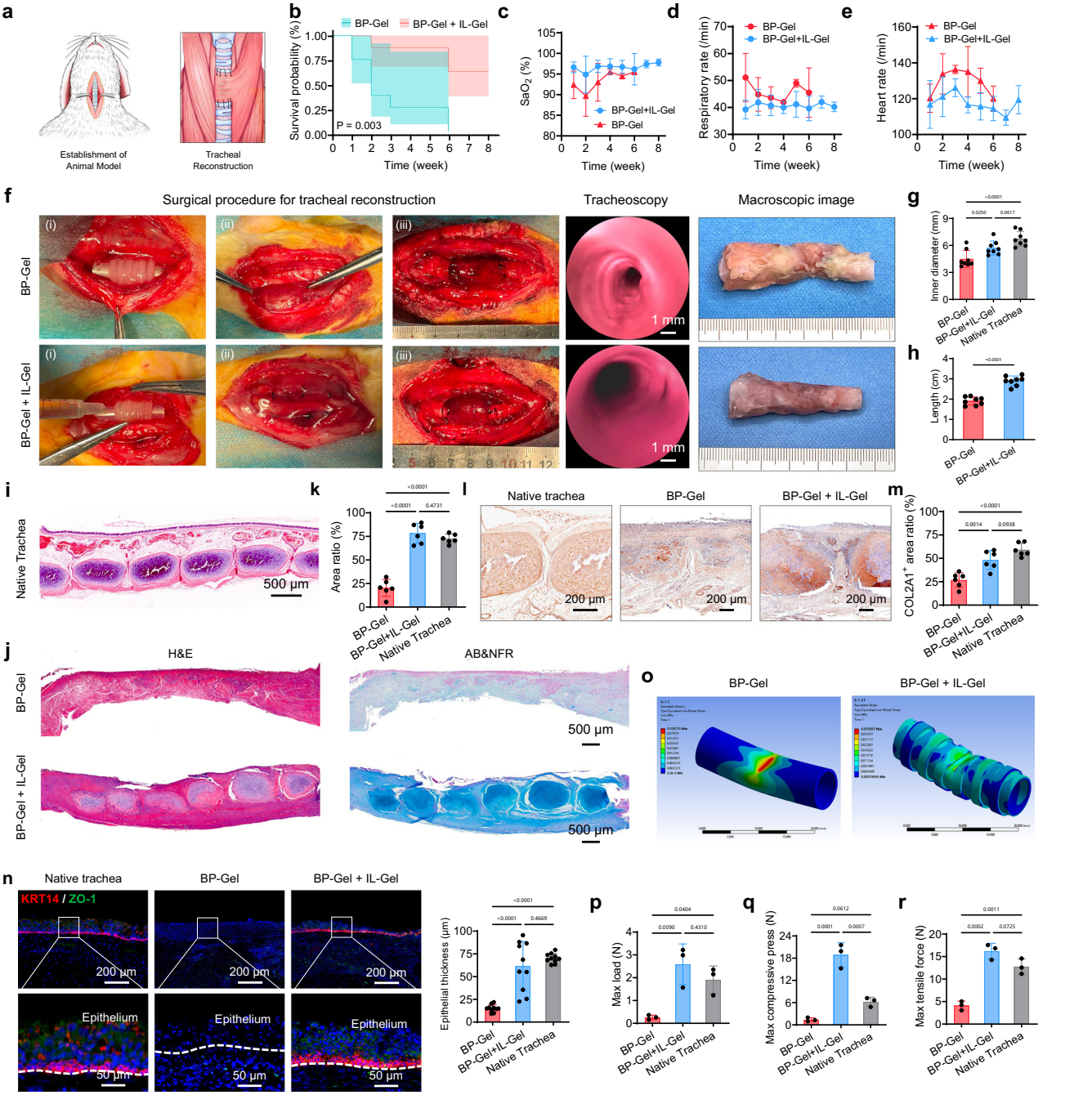

Fig. 5 | Segmental tracheal reconstruction mediated by DTE trachea. **a** Schematic of the rabbit tracheal defect model and subsequent DTE tracheal reconstruction. **b** Survival analysis of rabbits after various interventions. **c**–**e** Monitoring of SaO_2, respiration rate and heart rate ($n = 8$ individual samples per group). **f** Representative surgical procedure images, tracheoscopy images, and macroscopic image. Surgical procedure: (i) Multiple BioC rings that had been cultured in vitro for 4 weeks were superimposed and cast with IL-Gel to form a trachea substitute; (ii) The trachea substitute was implanted into the platysma muscle for further integration; (iii) The integrated trachea substitute was retrieved from the platysma muscle and subsequently implanted into a tracheal defect to reconstruct the trachea. **g** Quantitative analysis of the inner diameter of the reconstructed trachea ($n = 8$ individual samples per group). **h** Quantitative analysis of the reconstructed trachea length ($n = 8$ individual samples per group). **i** Representative H&E-stained micrograph of a native trachea. **j** Representative H&E and AB&NFR-stained micrographs of reconstructed tracheal. **k** Quantitative analysis of the proportion of cartilage area in reconstructed trachea ($n = 6$ random fields from 3 individual samples per group). **l**, **m** Representative COL2A1 IHC staining micrographs of reconstructed tracheas and quantitative analysis of the $COL2A1^+$ staining area ratio ($n = 6$ random fields from 3 individual samples per group). **n** Representative fluorescence micrographs of epithelial tissues labeled with KRT14 (red) and ZO-1 (green) and quantitative analysis of epithelial thickness. The dashed lines indicate the endothelial boundary ($n = 10$ random fields from 3 individual samples per group). **o** Finite Element Modeling simulation of longitudinal deformation and stress distribution under three-point bending. **p**–**r** Maximum load, compressive, and tensile forces of reconstructed tracheae ($n = 3$ individual samples per group). The data are expressed as the mean ± s.d. Data in (**b**) were analyzed by two-tailed log-rank test. Data in (**h**) were analyzed by two-tailed Student's t-test. Data in (**g**), (**k**), (**m**), (**n**), (**p**), (**q**), and (**r**) were analyzed by one-way ANOVA followed by Bonferroni's post hoc test. Source data is provided as a Source data file.

II cytoskeletal 5 (KRT5) and Forkhead box protein J1 (FOXJ1) demonstrated the presence of basal progenitors and ciliated cells, while AC-Tub marked mature cilia in the regenerated epithelium (Supplementary Fig. 12c). Quantitative analysis further confirmed that epithelial cilia coverage was significantly restored in the BP-Gel+IL-Gel group compared with BP-Gel alone (Supplementary Fig. 12d).

Moreover, vascularization between tracheal cartilage rings was markedly improved in the BP-Gel+IL-Gel group. H&E and α-SMA IHC staining revealed abundant and organized vessels comparable to those in native trachea, whereas the BP-Gel group displayed smaller and disordered vessels (Supplementary Fig. 12e). Quantitative analysis demonstrated that both vessel diameter and vascular area in the BP-Gel+IL-Gel group closely resembled native trachea but remained significantly greater than in the BP-Gel group (Supplementary Fig. 12f).

Finally, the results of force simulation analysis demonstrated that the degradation of BioC rings in the BP-Gel group induced stress concentration within the reconstructed tracheal lumen, leading to tracheal collapse and subsequent blockage (Fig. 5o and Supplementary Fig. 12g). Figure 5p, q and Supplementary Fig. 12h, i present the maximum loads and maximum compressive values of the reconstructed trachea in both groups, indicating that the mechanical strength in the BP-Gel+IL-Gel group was superior to that in the BP-Gel group. The results of tensile experiments further supported this finding (Fig. 5r and Supplementary Fig. 12j).

In summary, our exploited trachea substitute showed significantly higher survival rates, enhanced physiological stability, superior mechanical strength, improved cartilage preservation, and robust epithelial growth. These findings underscore its potential for functional and durable tracheal reconstruction.

Discussion

The restoration of organ function following failure due to disease, aging, or congenital conditions represents a significant scientific challenge. Organ transplantation remains among the most effective treatment options for many conditions. However, only 10% of organ transplant needs can be met. Regarding trachea lesions, 90% of adult primary tracheal tumors are malignant, with a 5-year overall survival rate of merely 31.7%[1,33]. Moreover, benign tracheal lesions can also impair ventilatory function and affect breathing[34]. For patients with these diseases, tracheal replacement is an important therapeutic alternative[1]. Recent advances in tissue engineering technologies have made the construction of tracheal replacements a promising solution to address the critical shortage of transplant donors.

The native trachea, comprising various tissue types including cartilage rings, blood vessels, and epithelium, exhibits a specific anatomical structure and spatial heterogeneity. The cartilage rings are arranged in an overlapping pattern and interconnected via interstitial connective tissue. The growth and development of these tissues involve dynamic regulation of the microenvironment, encompassing biochemical stimuli (such as hormone secretion and delivery, and growth factor interactions) and mechanical interactions (including tension and cell deformation)[5,35,36]. Therefore, in addition to restoring the structure, replicating the dynamic developmental processes of tissues is essential to ensure the formation of organ function. In this study, we proposed a DTE strategy for constructing tracheas and successfully developed a DTE trachea by integrating BioC rings with natural cartilage-like structures and properties and IL-Gel. The results revealed the ability of the constructed DTE trachea to mimic the environment during natural development, support tissue regeneration, provide mechanical strength, and regulate the immune response.

In the trachea, the cartilage rings are crucial for maintaining tracheal structural integrity and function due to their mechanical support. Early studies focused on constructing tracheal cartilage through engineered replacement solutions[37,38]. However, during ectopic implantation in vivo, these engineered cartilages may undergo varying degrees of degradation, leading to the dispersal of chondrocytes and ECM, which weakens the mechanical properties of the trachea and potentially causes trachea collapse[23]. To address this issue, most studies have suggested that the chondrocyte developmental environment influences the stability of the cartilage structure and conversely, destruction of the cartilage structure can adversely affect the chondrocyte developmental environment. Both factors interact reciprocally, collectively resulting in the in vivo degradation of engineered cartilage[39]. Based on these findings, recent research has attempted primarily to address the challenge of cartilage regeneration by simulating the native cartilage structure. For example, researchers have wrapped engineered cartilage in cartilage sheets to slow their degradation or constructed cartilage structures using three-dimensional printing to achieve a regular arrangement of collagen fibers[24,40].

However, current strategies remain limited to mimicking the gross morphology of native cartilage without activating endogenous pathways required for cartilage regeneration. Macrolevel structural designs are insufficient to influence matrix fiber orientation or cortical organization, and thus fail to reproduce the spatiotemporal stress patterns that guide cartilage development. Therefore, current engineered cartilage tissues remain suboptimal in terms of their retention and development in vivo[41]. Increasing evidence indicates that the native cartilage formation is closely related to its growth pattern and developmental stages[42,43]. During embryonic chondrogenesis, mesenchymal cells migrate, proliferate, and condense[44], followed by differentiation into chondrocytes under the regulation of key transcription factors such as SOX9[45] and signaling pathways including TGF-β and Wnt/β-catenin[46]. These coordinated events give rise to the cartilage primordium and establish the basis for matrix deposition and structural organization[46]. Beyond molecular regulation, the local biophysical environment plays an equally critical role. Intercellular signaling, mechanical environment, and heterogeneous oxygen distribution are critical factors in determining the biological function and microstructure of cartilage[9,25]. The present study proposes a key solution to this challenge. The ability of BP-Gel to promote chondrocyte aggregation and fusion, forming BioC tissue with a “cortex-medulla” structure and appropriate mechanical properties, represents a significant advance. Unlike conventional extracellular matrix-based hydrogels, BP-Gel based on PLGA-PEG-PLGA is a fully synthetic and well-characterized material with tunable physicochemical properties and minimal batch-to-batch variability. Moreover, its degradation profile and drug release kinetics can be precisely controlled, making it particularly suitable for applications in tissue engineering and regenerative medicine[16]. This attribute is crucial for maintaining the structural integrity of the trachea and resisting cartilage degradation. Meanwhile, within the BP-Gel, chondrocytes undergo aggregation and condensation at a significantly lower seeding density than required in conventional pellet cultures, while still supporting robust extracellular matrix deposition and cartilage-like tissue formation, thereby reducing cell consumption, minimizing culture costs, and enhancing translational potential.

In addition to the intrinsic growth and developmental status of cartilage, extrinsic environmental factors also play a critical role in determining its long-term persistence in vivo. Cartilage development requires a relatively low-metabolic niche, and excessive vascular invasion can accelerate cartilage degradation. The beneficial effect of IL-Gel arises not from a direct inhibition of angiogenesis, but from reshaping the inflammatory microenvironment to prevent pathological vascular overgrowth into cartilage. Meanwhile, IL-Gel promotes functional vascularization in the surrounding tissue, ensuring adequate nutrient supply without compromising cartilage integrity.

In addition to cartilage development, tracheal reconstruction also faces the challenge of regenerating complex tissues. Due to exposure to external physical and chemical irritants as well as pathogenic infections, the implantation of a trachea substitute can disrupt the

local immune microenvironment. This disruption leads to the accumulation of inflammatory cells, which produce various inflammatory factors (such as TNF-α, IL-1β, and IFN-γ), thereby disrupting local immune homeostasis. This hinders the migration of epithelial cells and the closure of the epithelial immune barrier. Additionally, developing a vascular system that regulates the immune microenvironment and maintaining the tracheal cartilage phenotype remains challenging[6,47]. To ensure the long-term functionality of a reconstructed trachea, it is essential to dynamically regulate the immune microenvironment to inhibit inflammation. Recent studies have shown that the regulation of the local immune regeneration microenvironment through biomaterials, active molecules, and physical-chemical stimuli is vital for achieving tissue regeneration. For example, modulating fibroblast inflammatory signals enhances the repair and regeneration of keratinized skin tissue[48], while the use of D-amino acids to activate adaptive immune responses facilitates wound healing and skin regeneration[49]. The reconstruction of the trachea is a complex tissue regeneration process involving the regulation of multiple developmental stages, thus requiring comprehensive modulation of the whole organ regeneration process within the same microenvironment. However, most current reports are limited to promoting the development of individual tissues. In this study, the integration of IL-Gel with BioC to create a polyfactorial niche significantly reduces local inflammation, facilitating epithelial migration, preventing cartilage degradation and maintaining cartilage phenotype. This also represents a significant advancement in tracheal reconstruction.

In vivo studies in a rabbit tracheal defect model confirmed that the DTE trachea composed of BioC and IL-Gel could achieve tissue development comparable to that of the native trachea, ensuring normal ventilation and survival in rabbit models. This represents a crucial breakthrough, as previous trachea substitutes often failed due to inadequate integration and vascularization, leading to compromised functionality and host rejection. The DTE approach introduced in this study provides a comprehensive solution by replicating the trachea's anatomical structure and creating a dynamic regenerative environment for different tissue types. The success of this approach in promoting long-term functionality post-transplantation suggests its potential applicability in the reconstruction of other complex organs, thus offering substantial technical and theoretical support for future translational efforts.

Additionally, this study has several limitations. First, this investigation represents only a preliminary exploration of the proposed strategy. The long-term prognosis of the rabbits after tracheal transplantation was not evaluated. Furthermore, this study did not extend the application of this strategy to large animal models. Future work will aim to apply this approach to repair a more extensive tracheal defect in large animals, such as goats or pigs, and to investigate the long-term outcomes.

In conclusion, this study employed BP-Gel to construct a DTE trachea. Its orthotopic transplantation in a rabbit model achieved satisfactory survival outcomes. The reconstructed bioengineered trachea exhibited good tissue development, native-like mechanical properties, and ventilation function. Future research should focus on further optimizing these niches and exploring their applications in other organ systems to expand the horizons of tissue engineering and regenerative medicine.

Methods

Study design

This study was designed to develop a DTE strategy for long-segment tracheal reconstruction using a BP-Gel. In the first stage, chondrocytes were cultured within BP-Gel to construct BioC rings, leveraging the hydrogel's dynamic percolation network to support cell migration, proliferation, and aggregation, thereby recapitulating an embryo-like chondrification process. In the second stage, BioC rings were assembled and sealed with IL-Gel to establish a regenerative niche that reduced local inflammation and promoted vascular and epithelial regeneration. The engineered trachea constructs were first matured in a heterotopic site and subsequently implanted into a rabbit long-segment tracheal defect model to evaluate structural, functional, and survival outcomes. The main reagents used for cell culture are listed in Supplementary Table 3.

Synthesis and characterization of materials

Synthesis of materials. PLGA-PEG-PLGA triblock copolymers were synthesized by ring-opening copolymerization. Polyethylene glycol (PEG, MW = 1500) and stannous octoate ($Sn(Oct)_2$) were procured from Sigma-Aldrich, whereas glycolide (GA) and D,L-lactide (LA) were supplied by Hangzhou Medzone Biotech Ltd. Initially, 15 g of PEG1500 was placed in a three-necked flask and dried under vacuum at 120 °C for 30 min. LA and GA were then introduced into the flask at a 7:2 molar ratio, followed by the addition of $Sn(Oct)_2$ (0.4% w/w) as a catalyst. The reaction was carried out at 140 °C under an inert atmosphere with constant stirring for 8 h. To remove unreacted monomers, the reaction mixture was subjected to a vacuum for an additional 30 min. The resulting copolymers were dissolved in water and precipitated at 80 °C, and this process was repeated 3 times. Finally, the product was obtained by freeze-drying.

Characterization of PLGA-PEG-PLGA. The chemical structure and composition ratio of the synthesized copolymer were analyzed via proton nuclear magnetic resonance (^{1}H NMR) spectroscopy on a 400 MHz NMR spectrometer (AVANCE III HD, Bruker). The ^{1}H NMR spectrum was obtained at room temperature with $CDCl_3$ (Sinopharm Chemical Reagent) as the solvent. The weight-average molecular weight (M_w) and molar mass dispersity ($Đ_m$) value of the copolymer were determined via a gel permeation chromatography (GPC, Agilent 1260) system. The analysis was performed at a flow rate of 1.0 mL/min with tetrahydrofuran (THF) as the mobile phase. Polystyrene standards were used as calibration references.

Dynamic light scattering (DLS). The PLGA-PEG-PLGA copolymers were first dissolved in deionized water to prepare a 10 wt% solution, which was subsequently diluted to concentrations of 1 wt% and 0.1 wt %. The hydrodynamic diameters of micelles formed by the copolymers at various temperatures were measured via a Zetasizer Nano ZS90 (Malvern). An argon ion laser with a wavelength of 532 nm served as the light source, and the measurements were conducted at a scattering angle of 90°. Prior to analysis, the samples were subjected to 1 min of ultrasonic treatment to minimize aggregation, followed by filtration through a 0.45 μm filter and equilibration at each temperature for 10 min.

Transmission electron microscopy. The copolymers were dissolved in deionized water at a concentration of 0.1 wt%, and the resulting solution was drop-cast onto copper grids. Some of the grids were air-dried at room temperature, while others were dried in an air bath at 37 °C. The dried copper grids were then observed and imaged using a transmission electron microscope (Tecnai G2 TWIN) at an accelerating voltage of 200 kV.

Phase diagram determination. The phase diagram of BP-Gel was determined via the vial inversion method[50]. Aqueous solutions of PLGA-PEG-PLGA at different mass ratios were prepared, and 0.5 mL of each solution was then transferred into 2-mL sample vials. The vials were immersed in a water bath with temperatures ranging from 15 to 50 °C. The temperature was increased in 0.5 °C increments. At each temperature, the samples were equilibrated for 10 min before being inverted. The sol–gel transition point was identified as the temperature at which the solution ceased to flow within 30 seconds upon inversion.

Rheological study. An advanced rotational rheometer (Kinexus, Malvern) was used to measure the storage modulus (G′) and loss modulus (G″) of BP-Gel across various temperatures and time intervals. The measurements were conducted with a strain amplitude of 1%, an angular frequency of 10 rad/s, and a heating rate of 1 °C/min. When the storage modulus (G′) exceeded the loss modulus (G″), the BP-Gel system was classified as being in a gel state; conversely, it was considered to be in a sol state when G′ was lower than G″.

Live/Dead and nuclear staining. After an incubation with 1 wt% PLGA-PEG-PLGA solution for the indicated durations, followed by staining with a Live/Dead Cell Imaging Kit (Invitrogen) according to the manufacturer's instructions. To improve image quality and provide clearer visualization of cell morphology and density, nuclei were counterstained with Hoechst 33342 (Yeasen). Fluorescence micrographs were acquired using a high-resolution fluorescence microscope.

In vivo BP-Gel formation and degradation. After sterilization of BP-Gel (25 wt%) via filtration, 0.2 mL of BP-Gel was subcutaneously injected into the dorsal region of ICR mice using a sterile syringe, resulting in the formation of an in situ hydrogel. At predetermined time points, the ICR mice were euthanized, and subsequent dissection was performed. The remaining BP-Gel was fully exposed and carefully peeled off, and the residual mass of BP-Gel was then measured.

Synthesis of fluorescent molecules. Rhodamine B was utilized as the fluorophore for fluorescence labeling of BP-Gel. Initially, 5 g of PLGA-PEG-PLGA was transferred into a round-bottom flask and dissolved in toluene to azeotropically remove any residual water. Subsequently, 1 g of Rhodamine B, 0.55 g of 1-ethyl-3-(3-dimethylaminopropyl) carbodiimide (EDCI), and 0.35 g of 4-dimethylaminopyridine (DMAP) were added. The reaction mixture was then dissolved in 20 mL of anhydrous dichloromethane and allowed to react under a nitrogen atmosphere for 36 hours. Following this, the mixture was washed with a 0.1 mol/L sodium bicarbonate ($NaHCO_3$) aqueous solution and extracted with anhydrous dichloromethane. The organic phase was dried over anhydrous sodium sulfate. After concentration via rotary evaporation, the product was precipitated using anhydrous ether, and the resulting precipitate was collected. After freeze-drying, the final product was attained.

For fluorescence labeling of IL-13, Cy5.5 was employed as the fluorophore. A total of 5 mg of Cy5.5 N-hydroxysuccinimide (NHS) was completely dissolved in 0.5 mL of dimethyl sulfoxide (DMSO) and then added dropwise to a solution of 20 mg of IL-13 in 0.1 mol/L $NaHCO_3$. The reaction was conducted in the dark at room temperature for 12 h. The mixture was subsequently subjected to dialysis using a dialysis bag with a MW cutoff of 3500 Da for 48 h, after which the solution was freeze-dried to yield the final product.

In vivo fluorescence imaging. After subcutaneous injection of Rhodamine B-labeled BP-Gel, ICR mice were monitored over time via an in vivo Xtreme (Bruker) multispectral optical imaging system. Anesthesia was maintained with isoflurane during the measurements. X-ray images were acquired with an exposure time of 1.2 s and an X-ray intensity of 45 kV. Fluorescence micrographs were captured in the same field of view, with an excitation wavelength of 560 nm, an emission wavelength of 600 nm, and an exposure time of 2 s. Similarly, after subcutaneous injection of IL-Gel containing Cy5.5-labeled IL-13, ICR mice were tracked over time using the same imaging system. The ICR mice were anesthetized with isoflurane, and X-ray images were captured under the same conditions as previously described. Fluorescence micrographs were also captured in the same field of view, using an excitation wavelength of 690 nm, an emission wavelength of 790 nm, and an exposure time of 2 s.

In vitro drug release. IL-Gel was prepared by mixing IL-4/13 at a concentration of 2 μg/mL with BP-Gel (PBS as the medium and the copolymer concentration of 25 wt%). Subsequently, 0.5 mL of IL-Gel was accurately transferred into the bottom of 10-mL test tubes (inner diameter of 14 mm) and incubated at 37 °C to facilitate the formation of a physical hydrogel. Next, 5 mL of PBS (pH 7.4, 37 °C) was added as the release medium. The in vitro release system was then placed in a shaking water bath at 37 °C with a fixed shaking rate of 50 rpm. At 1-day intervals, an aliquot of the release medium was withdrawn and replaced with an equal volume of fresh PBS. The amount of drug released into the medium was quantified using ELISA kits (Yes Biotech Laboratories Ltd., Canada). Each group was composed of quadruplicate samples.

Experimental animals

Nude mice (BALB/c-nu/nu, male, 6 weeks of age) and ICR mice (male, 6 weeks of age) were purchased from Shanghai Slake Laboratory Animal Co., Ltd. New Zealand white rabbits (male, 4–8 weeks of age) were purchased from Shanghai Jiagan Biotechnology Co., LTD. Sex was controlled by using only male animals to minimize variability in hormone-related physiological responses. In addition, pregnant ICR mice at embryonic days E12.5, E14.5, and E16.5 used for embryo collection were also purchased from Shanghai Slake Laboratory Animal Co., Ltd. All animal experiments were performed in compliance with the Guidelines for the Care and Use of Laboratory Animals. The procedures were approved by the Ethics Committee of Shanghai Pulmonary Hospital, and all institutional and governmental regulations on animal ethics were strictly followed. Mice were housed in individually ventilated cages under controlled conditions (12-h light/dark cycle, 22 ± 2 °C, 50 ± 10% relative humidity) with free access to standard chow and water.

In vitro construction and in vivo implantation of BioC

Chondrocyte extraction. Chondrocytes were extracted according to a previously described method[7]. Ear cartilage from 6-week-old New Zealand rabbits was harvested under aseptic conditions. After removing skin and fibrous membranes, cartilage was minced into 1 mm pieces and digested with 0.15% collagenase II for 24 h. The resulting suspension was filtered through a 70-μm strainer to isolate chondrocytes for culture.

Fabrication and in vitro culture of BioC. Chondrocytes were uniformly suspended with sterilized BP-Gel solution (12.5 wt%), which was filtered through 0.22 μm filters before use. Based on optimization experiments aimed at reducing chondrocyte usage while maintaining cartilage-forming capacity, the cell density was set at 4×10^6 cells/mL, which is substantially lower than that used in traditional culture conditions, to enable the formation of BioC. The chondrocyte-laden mixture was incubated at 37 °C for 30 min to complete the sol–gel transition, and then the chondrocyte medium containing 1% ITS+ Liquid Medium Supplement (ITS+, Sigma) and chondrogenic growth factors, including 50 ng/mL IGF-1 (PeproTech) and 10 ng/mL TGF-β1 (PeproTech), was added for culture. The culture medium was changed every other day.

In vivo implantation of BioC. After 4 weeks of in vitro culture, the matured BioC constructs or BioC rings were harvested and thoroughly rinsed with sterile PBS. For heterotopic evaluation, BioC samples were implanted into subcutaneous pockets in the dorsal region of nude mice or ICR mice to assess cartilage maturation, vascular invasion, and immune compatibility. For orthotopic transplantation, BioC rings were assembled with IL-Gel to form a tubular structure and then implanted into tracheal defect models in New Zealand rabbits. The implantation sites were carefully sutured, and animals were monitored postoperatively for survival, respiratory function, and potential complications. Tissues were harvested at predetermined time points for

histological, biochemical, and IHC analyses to evaluate the structural integrity, mechanical properties, and in vivo remodeling of BioC.

Construction of GelMA-chondrocyte composite and chondrocyte spheroids

Preparation of GelMA-chondrocyte composite. Chondrocytes were uniformly mixed with GelMA solution (10 wt%), which had been sterilized by filtration through 0.22 μm filters. The cell density was set at 4×10^6 cells/mL, consistent with that used for BioC. Other procedures for constructing the GelMA-chondrocyte composite were performed similarly to those for BioC.

Formation of chondrocyte spheroids. For the generation of chondrocyte spheroids, agarose microwell molds were prepared in six-well plates following the same approach as described in our previous study[7]. Approximately 1×10^5 chondrocytes were seeded per well, resulting in spheroids with an average diameter of 200 μm.

Construction and subcutaneous injection of IL-Gel

IL-4/13 was dissolved in BP-Gel (25 wt%) at a concentration of 20 μg/mL to obtain IL-gel. The resulting IL-gel was subsequently sterilized by filtration using 0.22 μm filters. Following sterilization, 0.2 mL of IL-Gel solution was subcutaneously injected into the dorsal region of ICR mice to facilitate the formation of an in situ gel. The ICR mice were euthanized via cervical dislocation at predetermined time points. The dorsal skin at the injection sites was carefully incised, and residual gels were photographed using a digital camera under standardized lighting conditions. Subsequently, the surrounding tissues containing the residual gels were harvested, fixed in 4% paraformaldehyde, and processed for histological and IHC analyses.

Construction of in vitro macrophage co-culture models

Cell sources. Endothelial cells were obtained from the human umbilical vein endothelial cell line PUMC-HUVEC-T1 (No. C01510C, Procell). Macrophages were derived from the RAW 264.7 cell line (No. SCC-211800, Servicebio). Primary chondrocytes and endothelial cells were isolated from New Zealand white rabbits. All cells were maintained at 37 °C in a humidified atmosphere containing 5% CO_2.

Isolation and culture of rabbit tracheal epithelial cells. The epithelial cells used for the ALI model were obtained from rabbit trachea, as previously described. Briefly, tracheal tissues were harvested following euthanasia and washed three times with PBS. The trachea was incubated at 37 °C for 30 min with dispase (Stem Cell, Canada), after which the mucosal layer was carefully separated and further digested overnight. The digested suspension was filtered through a 70 μm filter. The resulting epithelial cells were resuspended in epithelial culture medium consisting of DMEM (Gibco) and F-12 (Gibco) supplemented with 10% FBS (Gibco), 5 μM Y-27632 (Sigma), 10 ng/mL EGF (PeproTech), 5 μg/mL insulin (Sigma), 0.1 nM cholera toxin (Sigma), 250 ng/mL amphotericin B (Solarbio), and 10 μg/mL gentamycin (Gibco). Cells were cultured in 3 cm dishes at 37 °C in a humidified incubator with 5% CO_2, with medium changes three times per week. Epithelial cells were expanded to the third passage before seeding.

Transwell co-culture model. As illustrated in Fig. 3f, the Transwell co-culture system was used to investigate the interactions between macrophages and chondrocytes, endothelial cells, and epithelial cells. The Transwell setup facilitates the separation of cell types while permitting the exchange of soluble factors, thereby mimicking the in vivo microenvironment. Specifically, macrophages were seeded in the upper chamber of the Transwell system and embedded in various matrices, while chondrocytes, endothelial cells, or epithelial cells were seeded in the lower chamber. This setup allowed the investigation of the effects of macrophage-secreted factors on these cell types.

Air-liquid interface (ALI) co-culture model. In addition to the Transwell system, an ALI co-culture model was established to further examine the influence of macrophage-derived soluble factors on the differentiation and barrier function of epithelial cells (Fig. 3n). In this setup, macrophages were embedded in various matrices and cultured in the lower chamber, whereas epithelial cells were seeded on the upper insert membrane and maintained under ALI conditions to promote epithelial differentiation.

Establishment of ALI epithelial culture. Third-passage epithelial cells were seeded onto Matrigel (BD Biosciences)-coated Transwell and cultured until confluence. The apical medium was then removed to expose the cell layer to air, while the basal compartment was maintained with epithelial growth medium. This ALI culture promoted epithelial stratification and mucociliary differentiation, enabling functional assessment in the co-culture model.

Construction and in vivo implantation of BioC/IL-Gel composite

To investigate the role of IL-Gel in regulating the local microenvironment and its effect on cartilage integration, various *BioC* composites were constructed, as illustrated in Fig. 4a and Supplementary Fig. 11a. Specifically, the experimental setup consisted of four groups: GelMA, GelMA@Blk, BP-Gel, and BP@IL-Gel. Each composite was implanted into the platysma muscle of rabbits. Periodic sampling was performed post-implantation to analyze the histological characteristics and integration efficiency of the cartilage.

Segmental tracheal reconstruction in a rabbit tracheal defect model

First, multiple BioC rings that had been cultured in vitro for 4 weeks were positioned over a silicone tube, and IL-Gel was poured into the gaps between BioC rings to obtain a DTE trachea, as shown in Supplementary Fig. 12a. Next, the platysma muscle of rabbits was used to wrap the DTE trachea. After 4 weeks of vascularization in rabbits, the DTE trachea with a pedicled muscle flap was carefully stripped from the surrounding tissues, and the vascular network was closely monitored during the operation. After that, the silicone tube was removed from the DTE trachea, and the resulting trachea was cut to approximately 2 cm. After the construction of a segmental tracheal defect model in rabbits. A 6-0 absorbable suture was used to anastomose the detached native trachea with the trachea substitute. After tracheal anastomosis, the rabbits were treated prophylactically with penicillin for 7 days. The rabbits were sacrificed at predetermined time points, and the grafts were collected for further analysis.

Morphological analyses and mechanical tests

Photographic and morphological measurements. Photographs of all harvested tracheal samples were taken under standardized conditions. The widths and thicknesses of the samples were measured using a Vernier caliper, while the mass of each sample was determined with an electronic balance.

Compression testing. The compressive strength of the reconstructed trachea was evaluated using a biomechanical analyzer (Instron-6800, Norwood, USA) equipped with a 25 N load sensor. During compression testing, deformation was measured from the onset of loading until 50% of the maximal deformation was reached. The peak pressure within this range was recorded as the maximum pressure value.

Tensile testing. For tensile strength assessment, samples were subjected to uniaxial stretching until breakage. The tensile force recorded at the point of rupture was defined as the maximum sustainable tensile force of the reconstructed trachea.

Three-point bending testing. Flexural properties were assessed using a three-point bending test. Samples were positioned on two supporting anvils, with the loading point centrally located between them. A steadily increasing load was applied until either fracture occurred or the flexural angle exceeded 90°. The maximum load applied during the test was recorded as the maximum bending force.

Histological and IF&IHC analysis

Tissue fixation and section preparation. Samples were fixed in 4% paraformaldehyde for 24 h at room temperature, followed by a graded ethanol series for dehydration. Tissues were then embedded in paraffin and sectioned into 5-µm-thick slices using a microtome. The prepared sections were mounted onto glass slides for subsequent histological and IF analyses.

Histological staining. H&E staining was performed to evaluate overall tissue morphology and cellular distribution. AB&NFR and SO&FG staining were used to assess cartilage-specific ECM deposition, particularly glycosaminoglycans within the cartilage lacunae, with Fast Green serving as a counterstain for non-cartilaginous structures. SR staining was used to visualize collagen fibers. All stained sections were observed under a light microscope, and representative images were captured for comparison among groups.

IF and IHC staining. For antigen detection, tissue sections were deparaffinized, rehydrated, and subjected to antigen retrieval in citrate buffer (pH 6.0) at 95 °C for 15 min. After cooling, nonspecific binding was blocked with 5% bovine serum albumin (BSA) for 1 h at room temperature. Sections were then incubated overnight at 4 °C with specific primary antibodies (listed in Supplementary Table 4). For IF, sections were washed and incubated with fluorophore-conjugated secondary antibodies for 1 h at room temperature, counterstained with DAPI to visualize nuclei, and mounted with antifade reagent. Fluorescence micrographs were captured using an SP8 confocal microscope (Leica). For IHC, sections incubated with primary antibodies were subsequently treated with HRP-conjugated secondary antibodies (Abcam). Visualization was performed using diaminobenzidine (DAB) as the chromogen, and nuclei were counterstained with hematoxylin. Stained sections were observed under a bright-field microscope.

Quantitative analysis. Unless otherwise specified in the figure legends, quantification was performed by analyzing at least 5 randomly selected fields per section using ImageJ software to calculate the percentage of positive staining or fluorescence intensity.

Biochemical and molecular biology analysis

Sample preparation. Harvested tissue samples were weighed to determine wet weight, minced, and lyophilized for subsequent biochemical and molecular biology analyses. Lyophilized tissues were ground into fine powders and stored at −80 °C until further analysis.

DNA quantification. DNA content was measured using a total DNA quantitative assay kit (TIANGEN) according to the manufacturer's instructions. Briefly, tissues/cells were digested in lysis buffer (proteinase K-based) at 56 °C until complete digestion, followed by brief centrifugation to remove debris. DNA concentration and purity were measured with a NanoDrop spectrophotometer (Thermo Fisher Scientific) using A260 (with A260/A280 recorded for quality control).

GAG quantification. GAG content was determined by the dimethylmethylene blue (DMMB) method (Sigma), and concentrations were calculated using a chondroitin sulfate standard curve.

Quantitative real-time PCR (qRT-PCR). Total RNA was extracted with TRIzol reagent (Invitrogen), and cDNA was synthesized using a reverse transcription kit (Takara). qRT-PCR was performed with SYBR Green PCR Master Mix (Takara) on a real-time PCR system. GAPDH served as the internal reference gene, and relative expression levels were calculated by the $2^{-\Delta\Delta Ct}$ method. Primer sequences are provided in Supplementary Table 5.

Western blot (WB) analysis. Proteins were extracted using RIPA buffer containing protease inhibitors and quantified by BCA assay. Equal protein amounts were separated by SDS-PAGE, transferred to PVDF membranes, and blocked with 5% milk. Membranes were incubated overnight at 4 °C with primary antibodies, followed by HRP-conjugated secondary antibodies. Signals were detected with an ECL system (Bio-Rad), and band intensities were analyzed using ImageJ software.

Flow cytometry analysis

Cells were enzymatically digested and collected at a density of 1×10^5 cells per group, then resuspended in PBS containing 2% FBS and transferred into 1.5 mL Eppendorf tubes. To block nonspecific Fc receptor binding, 200 µL of Fc-Block reagent was added and incubated for 10 min at 4 °C, followed by washing with buffer to terminate the reaction. Subsequently, 2 µL of DCFH-DA fluorescent probe was added to each sample and incubated for 20 min at 4 °C in the dark. After incubation, cells were washed twice with PBS containing 2% FBS and resuspended in 200 µL buffer for detection. Flow cytometric analysis was performed using a FACSVerse flow cytometer (BD Biosciences, USA). The fluorescence intensity and percentage of positive cells were determined by comparison with the blank control group using FlowJo v10.6.2 software.

RNA sequencing and data analysis

Total RNA was extracted from tissue with TRIzol reagent (TaKaRa) and subsequently depleted of rRNAs via Ribo-Zero rRNA Removal Kits (Illumina) following the manufacturer's instructions. The RNA libraries were constructed from rRNA-depleted RNA using the TruSeq Stranded Total RNA Library Prep Kit according to the manufacturer's instructions. Libraries were controlled for quality and quantified via the BioAnalyzer 2100 system (Agilent Technologies, Inc.). Ten picometer libraries were denatured as single-stranded DNA molecules, captured on Illumina flow cells, amplified in situ as clusters, and sequenced for 150 cycles on an Illumina HiSeq Sequencer according to the manufacturer's instructions. Library preparation and high-throughput sequencing were performed by CloudSeq Biotech (Shanghai, China).

Statistical analysis

All statistical analyses were performed using GraphPad Prism 9.0. For comparisons between two groups, the unpaired two-tailed Student's t-test was used. For comparisons among three or more groups, one-way ANOVA with Tukey's post hoc test was applied. In cases involving two variables across multiple groups, two-way ANOVA followed by Bonferroni correction was employed. The log-rank test used for comparing Kaplan–Meier survival curves was performed as a two-sided test. All data are expressed as means ± standard deviations (s.d.), and p-values < 0.05 were considered statistically significant.

Ethical statement

All animal care, feeding, and research procedures were carried out following the Guidelines for the Care and Use of Laboratory Animals and were approved by the Ethics Committee of Shanghai Pulmonary Hospital (No. K23-107Y).

Reporting summary

Further information on research design is available in the Nature Portfolio Reporting Summary linked to this article.

Data availability

All data supporting the findings of this study are available within the article and its supplementary files. Any additional requests for information can be directed to, and will be fulfilled by, the corresponding authors. The raw RNA sequencing data generated in this study have been deposited in the Gene Expression Omnibus (GEO) under accession number GSE309417. Source data are provided with this paper.

References

1. Etienne, H. et al. Tracheal replacement. *Eur. Respir. J.* **51**, 1702211 (2018).
2. Wright, C. D. et al. Postintubation tracheal stenosis: management and results 1993 to 2017. *Ann. Thorac. Surg.* **108**, 1471–1477 (2019).
3. Guibert, N. et al. Treatment of post-transplant complex airway stenosis with a three-dimensional, computer-assisted customized airway stent. *Am. J. Respir. Crit. Care Med.* **195**, e31–e33 (2017).
4. Ali, S. R. & Mehta, A. C. Alive in the airways: live endobronchial foreign bodies. *Chest* **151**, 481–491 (2017).
5. Oliveira, J. F. D. et al. In *Tracheostomy* 11–22 (Springer, 2018).
6. Hollenhorst, M. I. et al. Bitter taste signaling in tracheal epithelial brush cells elicits innate immune responses to bacterial infection. *J. Clin. Invest.* **132**, e150951 (2022).
7. Tang, H. et al. A bioengineered trachea-like structure improves survival in a rabbit tracheal defect model. *Sci. Transl. Med.* **15**, eabo4272 (2023).
8. Xu, Y. et al. Biomimetic trachea engineering via a modular ring strategy based on bone-marrow stem cells and atelocollagen for use in extensive tracheal reconstruction. *Adv. Mater.* **34**, 2106755 (2022).
9. Yang, S. et al. Morphogens enable interacting supracellular phases that generate organ architecture. *Science* **382**, eadg5579 (2023).
10. Duda, G. N. et al. The decisive early phase of bone regeneration. *Nat. Rev. Rheumatol.* **19**, 78–95 (2023).
11. Laufer, E., Nelson, C. E., Johnson, R. L., Morgan, B. A. & Tabin, C. Sonic hedgehog and Fgf-4 act through a signaling cascade and feedback loop to integrate growth and patterning of the developing limb bud. *Cell* **79**, 993–1003 (1994).
12. Liu, Z., Wan, X., Wang, Z. L. & Li, L. Electroactive biomaterials and systems for cell fate determination and tissue regeneration: design and applications. *Adv. Mater.* **33**, e2007429 (2021).
13. Huang, G. et al. Functional and biomimetic materials for engineering of the three-dimensional cell microenvironment. *Chem. Rev.* **117**, 12764–12850 (2017).
14. Moroni, L. et al. Biofabrication strategies for 3D in vitro models and regenerative medicine. *Nat. Rev. Mater.* **3**, 21–37 (2018).
15. Tang, H., Sun, W., Chen, Y., She, Y. & Chen, C. Future directions for research on tissue-engineered trachea. *Bio-Des. Manuf.* **5**, 627–632 (2022).
16. Yu, L. & Ding, J. Injectable hydrogels as unique biomedical materials. *Chem. Soc. Rev.* **37**, 1473–1481 (2008).
17. Shi, J., Yu, L. & Ding, J. PEG-based thermosensitive and biodegradable hydrogels. *Acta Biomater.* **128**, 42–59 (2021).
18. Chen, X. et al. An injectable and active hydrogel induces mutually enhanced mild magnetic hyperthermia and ferroptosis. *Biomaterials* **298**, 122139 (2023).
19. Patel, M., Lee, H. J., Park, S., Kim, Y. & Jeong, B. Injectable thermogel for 3D culture of stem cells. *Biomaterials* **159**, 91–107 (2018).
20. Yu, J. et al. Single-dose physically cross-linked hyaluronic acid and lipid hybrid nanoparticles containing cyclic guanosine monophosphate-adenosine monophosphate eliminate established tumors. *ACS Nano* **18**, 29942–29955 (2024).
21. Sarmah, D. & Karak, N. Physically cross-linked starch/hydrophobically-associated poly(acrylamide) self-healing mechanically strong hydrogel. *Carbohydr. Polym.* **289**, 119428 (2022).
22. Tong, X. & Yang, F. Sliding hydrogels with mobile molecular ligands and crosslinks as 3D stem cell niche. *Adv. Mater.* **28**, 7257 (2016).
23. Ruscitto, A. et al. Lgr5-expressing secretory cells form a Wnt inhibitory niche in cartilage critical for chondrocyte identity. *Cell Stem Cell* **30**, 1179–1198.e1177 (2023).
24. Dai, M. et al. A well defect-suitable and high-strength biomimetic squid type II gelatin hydrogel promoted in situ costal cartilage regeneration via dynamic immunomodulation and direct induction manners. *Biomaterials* **240**, 119841 (2020).
25. Hou, M. et al. Dominant role of in situ native cartilage niche for determining the cartilage type regenerated by BMSCs. *Bioact. Mater.* **13**, 149–160 (2022).
26. Xiang, L. et al. Motion lubrication suppressed mechanical activation via hydrated fibrous gene patch for tendon healing. *Sci. Adv.* **9**, eadc9375 (2023).
27. Yu, L. et al. Comparative studies of thermogels in preventing postoperative adhesions and corresponding mechanisms. *Biomater. Sci.* **2**, 1100–1109 (2014).
28. Deng, J. et al. Versatile hypoxic extracellular vesicles laden in an injectable and bioactive hydrogel for accelerated bone regeneration. *Adv. Funct. Mater.* **33**, 2211664 (2023).
29. Zhang, H. et al. Maintaining hypoxia environment of subchondral bone alleviates osteoarthritis progression. *Sci. Adv.* **9**, eabo7868 (2023).
30. Zhang, Y. et al. Dual functions of microRNA-17 in maintaining cartilage homeostasis and protection against osteoarthritis. *Nat. Commun.* **13**, 2447 (2022).
31. Castilho, M., Mouser, V., Chen, M., Malda, J. & Ito, K. Bi-layered micro-fibre reinforced hydrogels for articular cartilage regeneration. *Acta Biomater.* **95**, 297–306 (2019).
32. de Roy, L. et al. Structure-function of cartilage in osteoarthritis: an ex-vivo correlation analysis between its structural, viscoelastic and frictional properties. *Acta Biomater.* **190**, 293–302 (2024).
33. Nilssen, Y. et al. Tracheal cancer: a rare and deadly but potentially curable disease that also affects younger people. *Eur. J. Cardiothorac. Surg.* **64**, ezad244 (2023).
34. Boogaard, R. et al. Tracheomalacia and bronchomalacia in children: incidence and patient characteristics. *Chest* **128**, 3391–3397 (2005).
35. Furlow, P. W. & Mathisen, D. J. Surgical anatomy of the trachea. *Ann. Cardiothorac. Surg.* **7**, 255 (2018).
36. Samat, A. A., Hamid, Z. A. A., Yahaya, B. H. & Mariatti Jaafar, M. In *Advances in Experimental Medicine and Biology* (2022).
37. Xia, D. et al. Tissue-engineered trachea from a 3D-printed scaffold enhances whole-segment tracheal repair in a goat model. *J. Tissue Eng. Regen. Med.* **13**, 694–703 (2019).
38. Xu, Y. et al. Photocrosslinked natural hydrogel composed of hyaluronic acid and gelatin enhances cartilage regeneration of decellularized trachea matrix. *Mater. Sci. Eng. C* **120**, 111628 (2021).
39. van Gastel, N. et al. Lipid availability determines fate of skeletal progenitor cells via SOX9. *Nature* **579**, 111–117 (2020).
40. Li, D. et al. Stable subcutaneous cartilage regeneration of bone marrow stromal cells directed by chondrocyte sheet. *Acta Biomater.* **54**, 321–332 (2017).
41. Daly, A. C. & Kelly, D. J. Biofabrication of spatially organised tissues by directing the growth of cellular spheroids within 3D printed polymeric microchambers. *Biomaterials* **197**, 194–206 (2019).
42. Decker, R. S., Koyama, E. & Pacifici, M. Articular cartilage: structural and developmental intricacies and questions. *Curr. Osteoporos. Rep.* **13**, 407–414 (2015).
43. Bhattacharjee, M. et al. Tissue engineering strategies to study cartilage development, degeneration and regeneration. *Adv. Drug Deliv. Rev.* **84**, 107–122 (2015).
44. Yang, B. et al. Recapitulating hypoxic metabolism in cartilaginous organoids via adaptive cell-matrix interactions enhances histone

lactylation and cartilage regeneration. *Nat. Commun.* **16**, 2711 (2025).
45. Yang, W. & Lefebvre, V. PTPN11 in cartilage development, adult homeostasis, and diseases. *Bone Res.* **13**, 53 (2025).
46. Woods, J. P., Rackley, A., Kwon, H. R. & Olson, L. E. PDGFRα signaling regulates cartilage and fibrous tissue differentiation during synovial joint development. *Nat. Commun.* **16**, 4041 (2025).
47. Minamoto, K. & Pinsky, D. J. Recipient iNOS but not eNOS deficiency reduces luminal narrowing in tracheal allografts. *J. Exp. Med.* **196**, 1321–1333 (2002).
48. Liu, S. et al. A tissue injury sensing and repair pathway distinct from host pathogen defense. *Cell* **186**, 2127–2143.e2122 (2023).
49. Griffin, D. R. et al. Activating an adaptive immune response from a hydrogel scaffold imparts regenerative wound healing. *Nat. Mater.* **20**, 560–569 (2021).
50. Yu, L., Chang, G., Zhang, H. & Ding, J. Temperature-induced spontaneous sol–gel transitions of poly(D,L-lactic acid-co-glycolic acid)-b-poly(ethylene glycol)-b-poly(D,L-lactic acid-co-glycolic acid) triblock copolymers and their end-capped derivatives in water. *J. Polym. Sci. Part A: Polym. Chem.* **45**, 1122–1133 (2007).

Acknowledgements

This study was supported by the Noncommunicable Chronic Diseases-National Science and Technology Major Project (no. 2024ZD0529000 (C.C.), 2024ZD0540700 (H.T.), and 2023ZD0516200 (W.S.)), the National Key Research and Development Program of the Ministry of Science and Technology no. 2022YFC2407401 (C.C.) and no. 2024YFC3044600 (C.C.), the National Natural Science Foundation of China (NSFC) no. 81770091 (C.C.), the Science and Technology Commission of Shanghai Municipality no. 24YF2735500 (H.T.), the Shanghai Municipal Health Commission no. 2023ZZ02025 (C.C.), the Shanghai Pulmonary Hospital no. FKJY2405 (H.T.), and no. FKCY2406 (H.T.), the Clinical Research Foundation of Shanghai Pulmonary Hospital no. FKLY20007 (C.C.) and no. SKPY2021005 (L.Z.), the Ningbo Top Medical and Health Research Program no. 2022030208 (G.Z.).

Author contributions

H.T., H.W., and W.S. designed the study and conducted data curation and analysis. H.T. oversaw all experiments and contributed to cell experiments, animal surgery, sample collection, histological analysis, mechanical and biochemical testing. H.W. and W.S. contributed to cell experiments, animal surgery and sample collection. Y.C. contributed to RNA sequencing, data curation and analysis. H.W. and Y.W. contributed to experimental material fabrication, characterization, data collation and analysis. Z.P., Q.B., W.L., and L.W. contributed to cell experiments, animal studies and data analysis. Z.P., Q.B., Y.H., M.Y., G.Z., and L.Z. contributed to animal surgery, data collation and validation. Y.S. and X.H. contributed to data validation and writing and review of the manuscript. J.D. and K.L. contributed to the manuscript's writing and review. C.C. and L.Y. supervised the study and contributed to the manuscript's design, writing and review.

Competing interests

The authors declare no competing interests.

Additional information

Supplementary information The online version contains supplementary material available at https://doi.org/10.1038/s41467-025-67580-0.

Correspondence and requests for materials should be addressed to Weiyan Sun, Lin Yu or Chang Chen.

Peer review information *Nature Communications* thanks Tendy Chiang, and the other, anonymous, reviewer(s) for their contribution to the peer review of this work. A peer review file is available.